ELSEVIER

Contents lists available at ScienceDirect

Applied Ocean Research

journal homepage: www.elsevier.com/locate/apor



Research paper



Reduced Order Modeling (ROM) based method for the two-dimensional water exit problem using snapshot Proper Orthogonal Decomposition (POD) and CFD simulations

Xupeng Sui ^b, Kamal Djidjeli ^b, Zhe Sun ^{a,*}, Jing Tang Xing ^b

- ^a School of Naval Architecture and Ocean Engineering, Dalian University of Technology, Dalian, 116024, China
- ^b CED Group, Boldrewood Campus, University of Southampton, Southampton, SO16 7QF, United Kingdom

ARTICLE INFO

Keywords:
Water exit
Snapshot POD
Reduced order modeling
Computational fluid dynamics

ABSTRACT

In this paper, the concepts of snapshot Proper Orthogonal Decomposition (POD) and Reduced Order Modeling (ROM) are combined (referred to the POD-ROM method) to solve the two-dimensional (2D) water exit problem. Attention is paid to the pressure distribution along the wetted surface of the body. Computational Fluid Dynamics (CFD) simulations are employed to obtain high-fidelity data on pressure distribution. After applying snapshot POD, it is found that two POD basis modes for the wedge model and three modes for the ship section model are adequate to capture dynamic features of the pressure distribution without losing too much detail. It can also be observed that neither the body motion state nor the initial immersion condition influences all POD functions of the wedge model, but the temporal POD functions of the ship section model are significantly dependent on the initial immersion height. A group of empirical formulae is provided to deal with this issue. The validity and reliability of our POD-ROM method are assessed by investigating water exit cases with both constant and time-varying body accelerations. In this context, after deriving POD functions of any given 2D body from a single CFD simulation, predictions of the pressure distribution along the body can be facilitated for further water exit cases.

1. Introduction

Initial research on the water exit problem concentrated on typical hydrodynamic scenarios where an aircraft is ditching and high-speed vessels are sailing on the free surface. The resolution of hydrodynamic loads on the body surface was greatly facilitated by the so-called "2D+T" concept proposed by Fontaine and Cointe (1997), where a complicated three-dimensional (3D) issue was approximated by a series of two-dimensional (2D) water entry and exit problems. The well-known research by Kaplan (1987) and Kaplan (1992) can be regarded as the pioneering work, where the 2D water exit problem was comprehensively investigated using analytical methods. In his study, the total hydrodynamic force acting on 2D bodies interacting with liquid was decomposed into two components: the slamming term and the added mass term. Meanwhile, according to the statements from Kaplan (1987) and Kaplan (1992), the slamming term was significantly suppressed during the water exit phase, which indicates that the body acceleration played a dominant role in the force computation. Similar arguments can also be observed in the work of Korobkin (2013), who proposed a linear analytical model by introducing several assumptions and subsequently investigated the variation of the wetted width of 2D bodies. Korobkin et al. (2017) further applied this approach to bodies with varying contours and then considered nonlinear factors to improve the accuracy of prediction results. Furthermore, a semi-analytical model was proposed by Tassin et al. (2013) using the von Karman model and provided predictions that showed satisfactory agreement with results from other literature.

In addition to conventional analytical models, computational power has recently been utilised to address such hydrodynamic problem. For example, Del Buono et al. (2021) introduced a hybrid BEM-FEM approach to improve the stability of numerical simulations and revealed that the effects of gravity were significant during the water exit phase. Rajavaheinthan and Greenhow (2015) used the boundary element method to solve the water exit problem, focusing on symmetric and asymmetric wedges, truncated wedges and boxes elevated directly from the water. Sui et al. (2024) combined the concept of load

E-mail address: zsun@dlut.edu.cn (Z. Sun).

^{*} Corresponding author.

decomposition and the computational fluid dynamics (CFD) method, and then carried out investigations on the forces acting on bodies under two different scenarios: direct water exit and continuous water entry and exit. In his work, the maximum immersion depth played an important role in the evolution of the force, which indicates that it is rather prohibitive to accomplish fast predictions for numerous cases with different maximum immersion depths. In this context, considering the practical application in the field of maritime engineering, we are motivated to figure out an improved method to solve this issue.

Meanwhile, although powerful computational resources can provide results with a certain degree of precision, high cost prevents this tool from widespread use in practical research, particularly for complicated problems involving a large number of dimensions. In this case, the socalled snapshot Proper Orthogonal Decomposition (POD) was proposed by Lumley (1967) and Sirovich (1987a) and then first used to deal with nonlinear turbulent flows. Specifically, a high-fidelity database is constructed by collecting a sequence of snapshots containing detailed physical information and then decomposed into a group of POD modes and their corresponding time coefficients, which represent spatial and temporal information, respectively. From the perspective of energy proportion, the highest ranked modes are identified as the dominant POD basis modes, while the lower ranked modes are ignored. In this case, the infinite dimensionality of a given complex problem can be reduced to a finite one represented by a limited number of POD modes, which is consistent with the concept of Reduced Order Modeling (ROM). In this paper, we will refer to this approach as the POD-ROM method.

There is no doubt that the POD-ROM method has an advantage in the resolution of hydrodynamic problems with strong nonlinear factors. Hilberg et al. (1994) used the POD-ROM method to analyse the turbulent flow developing periodic structures in a narrow channel and reconstructed the velocity field by identifying 10 POD basis modes out of 180. Meanwhile, Sen et al. (2007) also employed this approach to identify POD basis modes from numerical results of a turbulent channel flow with rough walls and performed both one- and two-dimensional POD analysis. The one-dimensional case showed that the convergence of POD was slower for the rough wall compared to the smooth wall, while the two-dimensional case indicated that the length scales of dominant structures were strongly modified by the roughness. In addition, Olbrich et al. (2021) found the characteristics of the slug flow in a confined horizontal pipe using the snapshot POD method in combination with an extra mode coupling algorithm and then further investigated the influence of the pipe section size. Moreover, Druault and Chaillou (2007) focused on the 3D in-cylinder mean flow field reconstructed by POD basis modes recognised from the PIV measurement database. In terms of the flow control, Siegel et al. (2006) identified a group of POD basis modes from a numerical database and then used them to estimate the flow state through a feedback controller. The case of a 2D circular cylinder wake was demonstrated in their work. Liberge and Hamdouni (2010) also employed this method for a nonlinear fluid-structure interaction (FSI) problem where transient flows moved around an oscillating cylinder. The dominant POD basis modes were tested on a high Reynolds number case and verified to be able to provide accurate predictions. Inspired by the effectiveness and efficiency of the POD-ROM method, we are aimed at using it to investigate the pressure distribution along the wetted surface of the body experiencing direct water exit, so that not only predictions of hydrodynamic load can be facilitated, but also tedious and time-consuming theoretical calculations or numerical simulations can be avoided.

Based on the above context, the structure of this paper is as follows: First, theoretical backgrounds related to the water exit and the concept of POD-ROM are shown in Section 2. Then, in section 3, the body models for investigation and the CFD strategy used to construct the high-fidelity database are stated. Subsequently, Section 4 consists of two separate parts presenting and analysing the POD functions for different body models, including the mean mode, the dominant POD basis modes and the corresponding time coefficients. Verification cases are then carried out in Section 5, followed by further discussions to identify the characteristic evolution patterns for temporal POD functions. Finally, the conclusions of our research are drawn in section 6.

2. Theoretical backgrounds

2.1. Pressure distribution of the body directly exiting the water

First, a theoretical model on the pressure distribution of a 2D rigid and symmetric body directly exiting the water is briefly presented below, referring to the work of Korobkin (2013) and Korobkin et al.

An overall sketch of water exit is illustrated in Fig. 1. In detail, shown as Fig. 1(a), the body is placed with an initial immersion height d_0 below the calm free surface. The parameter r_{ic} , defined as the ratio of the initial immersion height d_0 and the total body height H (namely $r_{ic} = d_0/H$), is introduced here to represent the immersion condition of the body at the beginning of movement. Note that r_{ic} is never over 1 in this research, ensuring that the upper boundary of the body always remains dry. The horizontal plane of the calm free surface and the vertical symmetric axis of the body establish the Cartesian coordinate system, and their intersection is designated as the origin point O. The body is then subjected to an upward motion with an initial speed of 0 and a prescribed acceleration a(t) which is positive during acceleration motion while negative during deceleration. It is worth mentioning that the entire water exit process we study here terminates when the bottom point of the body reaches the origin point O. Moreover, it should be noted that the parameter c denotes the wetted half-width of the body and is equal to c_0 at the initial moment.

Using the theoretical method to solve this problem, some assumptions have to be introduced as follows: (i) the contour of the body tends to be blunt, namely the width dimension of the body is much larger than its height dimension; (ii) the acceleration of the body is always much larger than the gravitational acceleration |g| ($|g|=9.8 \text{ m/s}^2$); (iii) surface tension, fluid viscosity and gravity are never taken into account; (iv) the duration of the entire water exit process is short; (v) cavitation never occurs at the interface between the body and the water. More details can be found in the work of Korobkin (2013) and Korobkin et al. (2017).

Based on the aforementioned context, the governing equations of the flow over the whole computational domain can be described as:

$$\begin{cases} \Delta \varphi = 0 & (z < 0) \\ \varphi_t = 0 & (z = 0, |y| > c(t)) \\ \varphi_z = \nu(t) & (z = 0, |y| < c(t)) \\ \varphi \rightarrow 0 & (y^2 + z^2 \rightarrow \infty) \end{cases} \tag{1}$$

where φ is the velocity potential function of the flow and ν is the body velocity. Using the Bernoulli equation, the pressure distribution p along the wetted surface of the body can then be expressed analytically as (Korobkin et al., 2017):

$$p(\mathbf{y}, \varsigma(\mathbf{y}, t), t) = p_{tinear} + p_{non-linear} = -\rho a(t) \sqrt{c^2(t) - \mathbf{y}^2} - \rho \left(a(t) (\varsigma(\mathbf{y}, t) - \varsigma(c, t)) - 0.5 \mathbf{v}^2(t) \right), \quad (|\mathbf{y}| < c(t))$$
(2)

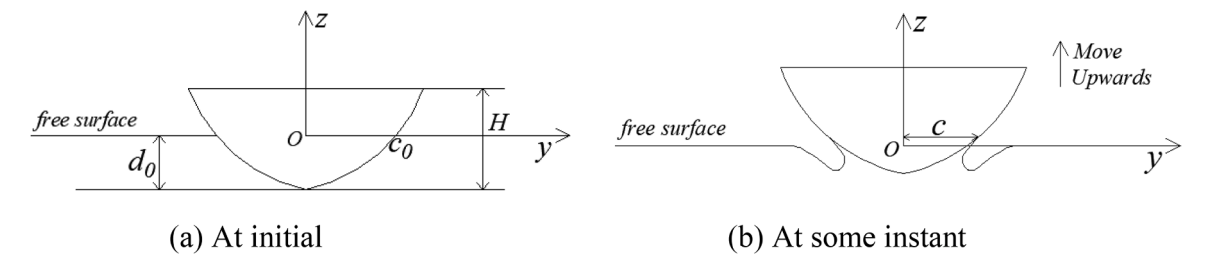


Fig. 1. Overall sketch of a 2D rigid and symmetric body directly exiting the water.

where $p_{linear} = -\rho a(t) \sqrt{c^2(t) - y^2}$ and $p_{non-linear} = -\rho \left(a(t)(\varsigma(y,t) - \varsigma(c,t)) - 0.5 v^2(t)\right)$ represent the linear and nonlinear components of the pressure acting on the body, respectively; $\varsigma(y,t)$ is the shape function of the body.

In accordance with the research by Sui et al. (2024), who also investigated the water exit problem using the theoretical model mentioned above, the pressure component associated with body velocity is neglected due to the short duration of the water exit. Subsequently, non-dimensionalisation is applied throughout the whole computational domain, which leads to:

$$p(\sigma,\xi) = \rho a(\xi) d_0 P_A(\sigma,\xi) \tag{3}$$

$$P_A(\sigma,\xi) = \frac{-\sqrt{c^2 - (c\sigma)^2} - \varsigma(c\sigma,\xi) + \varsigma(c,\xi)}{d_0}$$
(4)

where $\sigma=y/c$ is the non-dimensional horizontal coordinate of a point on the wetted surface of the body, ranging from 0 to 1; $\xi=d/d_0$ is the non-dimensional displacement of the body, also ranging from 0 to 1; $P_A(\sigma,\xi)$ is a non-dimensional coefficient, which is independent of the motion state of the body if its shape is specified. It should be noted that the non-dimensional displacement of the body ξ is used as the parameter representing the time domain.

By observing Eqs. (3) and (4), it can be expected that the emphasis on addressing the water exit problem shifts from the dynamic characteristics of the flow around the body to the evolution of the non-dimensional coefficient $P_A(\sigma,\xi)$. In terms of $P_A(\sigma,\xi)$, the wetted half-width c plays a crucial role. Some well-known analytical models provide their own formulae on the determination of c (see the work of Korobkin (2013) and Korobkin et al. (2017)), but nearly all of them are rather difficult and complicated, particularly when applied to curve-shaped bodies. Recently, an innovative method was proposed by Sui et al. (2024), who combined the concept of load decomposition with the CFD simulation method to overcome the challenges of solving c analytically and then achieved force predictions with a certain degree of accuracy and efficiency. However, as stated by Sui et al. (2024), for the ship section model with a complicated contour, the initial immersion height d_0 significantly influenced the development of hydrodynamic force, thereby constraining the applicability of this method in maritime engineering, especially when dealing with a large number of water exit cases. Motivated by this, we are intended to address this issue by using the POD-ROM method, focusing on the dynamic variation of pressure distribution along the wetted body surface. Fundamental information and analysis procedures based on the POD-ROM method are presented in the next subsection.

2.2. POD-ROM method for the pressure distribution calculation

In this paper, the so-called snapshot POD proposed by Sirovich (1987a, 1987b, 1987c) is employed to calculate the pressure distribution along the wetted surface of the body. The first step is to establish the database, which includes a series of snapshots that comprise pressure information captured at a certain time interval. Considering a system

within a limited spatial and temporal domain, the pressure field ${\bf P}$ can be represented in matrix form:

$$\mathbf{P} = [\mathbf{p}_1, \mathbf{p}_2, ..., \mathbf{p}_b] \cdot \mathbf{P} \in \mathbf{R}^{m \times b}$$
 (5)

where \mathbf{p}_i denotes pressure information at the ith snapshot, and m represents the number of spatial nodes while b means the number of snapshots. In order to leave pressure data containing deviations from the average, the mean mode $\overline{\mathbf{p}}$ is calculated using

$$\overline{\mathbf{p}} = \frac{1}{b} \sum_{k=1}^{b} \mathbf{p}_k \tag{6}$$

Subsequently, the fluctuation matrix $\widetilde{\mathbf{P}}(x,t)$ is computed by subtracting the mean as:

$$\widetilde{\mathbf{P}} = [\widetilde{\mathbf{p}}_1, \widetilde{\mathbf{p}}_2, ..., \widetilde{\mathbf{p}}_b] \cdot \widetilde{\mathbf{p}}_i = \mathbf{p}_i - \overline{\mathbf{p}}$$
(7)

The covariance matrix is then constructed as $\mathbf{W} = \widetilde{\mathbf{P}}\widetilde{\mathbf{P}}^{\mathrm{T}}/b$, where $\mathbf{W} \in \mathbf{R}^{m \times m}$. The eigenvalues $\Lambda_{m \times m} = diag[\lambda_1, \lambda_2, ..., \lambda_m]$ (sorted $\lambda_1 \geq \lambda_2 \geq ... \geq \lambda_m$) and the corresponding eigenvectors $\mathbf{Y} = [\gamma_1, \gamma_2, ..., \gamma_m]$ of the covariance matrix \mathbf{W} can be obtained by solving the following eigenvalue problem:

$$\widetilde{P}\widetilde{P}^{T}Y = \Lambda Y. \tag{8}$$

Consequently, the matrix $\Psi = [\psi_1, \psi_2, ..., \psi_m]$ containing a total of m spatial basis modes can be calculated by

$$\Psi = \widetilde{\mathbf{P}}^{\mathrm{T}} \mathbf{Y} \Lambda^{-1/2} \tag{9}$$

while the time coefficient matrix corresponding to each basis mode $A = [a_1, a_2, ..., a_m]$ can be determined using

$$\mathbf{A}^T = \mathbf{\Psi}^T \widetilde{\mathbf{P}}.\tag{10}$$

It should be mentioned that all POD basis modes are sorted from the perspective of energy proportion, which indicates that the 1st basis mode ψ_1 contains the most energy among all modes. The energy proportion ω that the ith basis mode ψ_i contributes to the entire system can be written as:

$$\omega_{i} = \frac{|\lambda_{i}|}{\sum_{k=1}^{m} |\lambda_{k}|} \times 100\%, \quad i = 1, 2, ..., m$$
(11)

The first n basis modes (n < m) are identified as the dominant basis modes by satisfying

$$\frac{\sum\limits_{k=1}^{n}|\lambda_k|}{\sum\limits_{k=1}^{m}|\lambda_k|}\approx 1.0\;,\;n\leq m \tag{12}$$

or

$$\sum_{k=1}^{n} \omega_k \approx 100\%, \ n \le m \tag{13}$$

Finally, to carry out the reconstruction of the pressure field P, the mean mode \overline{p} , the dominant POD basis modes $\Psi = [\psi_1, \psi_2, ..., \psi_n]$ and their corresponding time coefficients $A = [a_1, a_2, ..., a_n]$ are assembled and then formulated as:

$$\mathbf{P} \approx \overline{\mathbf{p}} + \sum_{k=1}^{n} \psi_k \mathbf{a}_k \tag{14}$$

As Eq. (3) and related arguments shown in Section 2.1, attention is paid to the development of the non-dimensional coefficient P_A , which evolves in both spatial and temporal domains. In this case, the snapshot POD will be applied to the database containing the results of P_A . Moreover, the non-dimensionalisation introduced in Section 2.1 is still used. Consequently, Eq. (14) can be rewritten in scalar form as:

$$p(\sigma,\xi) = \rho a(\xi) d_0 \left(\overline{P}(\sigma) + \sum_{k=1}^n \psi_{p,k}(\sigma) a_{p,k}(\xi) \right)$$
 (15)

where \overline{P} , $\psi_{p,i}$ and $a_{p,i}$ are three non-dimensional parameters, representing the mean mode, the ith POD basis mode and its corresponding time coefficient, respectively. In this paper, we refer to these parameters as POD functions. In addition, it can be easily observed that \overline{P} and $\psi_{p,k}$ are spatial functions while $a_{p,k}$ is a temporal function.

Eq. (15) suggests that the issue with a full order of m is projected onto a subspace spanned by n dominant POD basis modes, and the accurate pressure field can be reconstructed using just these modes. This practice coincides with the essence of ROM, namely the order reduction with preserving crucial dynamic features. Due to the non-dimensional coefficient P_A being independent of the motion state of the body, the water exit problem involving diverse upward motions of the body can be efficiently solved using the specialised POD functions, which are preobtained from only a few times of computation. As a result, while dealing with potential water exit cases, the pressure distribution along the wetted surface of the body can be fast and accurately predicted using our proposed POD-ROM method (namely Eq. (15)), once the initial immersion height d_0 is identified. This practice greatly prevents laborious and time-consuming theoretical calculations or numerical simulations. The factors that determine POD functions comprehensively investigated in Section 4.

As mentioned at the beginning of this subsection, it is of great meaning to construct the high-fidelity database. In this paper, the CFD simulation method is employed to evaluate the pressure distribution along the wetted surface of the body and then derive the results of the non-dimensional coefficient P_A with a certain degree of accuracy. Detailed information on the CFD strategy is given in Section 3.

3. CFD strategy and verification

The commercial CFD software STAR-CCM+ is used in this paper to obtain high-fidelity results of the pressure distribution along the wetted $\,$

surface of the body. A few analogous 2D water entry and exit problems have been examined using CFD methods in the existing literature (refer to Sun et al. (2022) and Sui et al. (2024)). In this case, we are motivated to create our numerical models informed by their setups, including CFD solvers and physical models. More specifically, in all numerical simulations, the Reynolds-Averaged Navier-Stokes (RANS) model is used to govern the flow across the whole computational domain, while the Volume of Fluid (VOF) technique is applied to capture the free surface between the air and the water phases. Moreover, the realisable $k-\varepsilon$ model is selected because the fluid viscosity is too weak to be considered in the problem studied here, and this type of $k-\varepsilon$ model offers greater flexibility compared to the standard one. It should also be noted that gravity is always excluded in all simulation cases.

Two different types of 2D rigid and symmetric body models are investigated in this paper. In detail, one is the typical wedge model with a deadrise angle of 30 degrees, while the other is the practical ship section model derived from the work of Aarsnes (1996). Additional information on model outlines and dimensions can be found in Table 1.

The interaction between the body and the water is then solved using the finite volume method. In addition, the boundary conditions for all sides of the computational domain are designated as "rigid wall", with the exception of the upper side, which is replaced by a "pressure outlet". This indicates that the pressure at the top remains constant and is equivalent to the standard atmospheric pressure. A general sketch of the whole computational domain is presented in Fig. 2, taking the wedge model as an example. In the meantime, the dimensions of the domain for each model examined in this paper are shown in Table 2.

Concerning the mesh distribution, we also follow the example set by Sui et al. (2024). Firstly, the whole computational domain is discretised using a specific type of structured mesh, called "trimmed cell meshes", supplied by STAR-CCM+. In the 2D scenario studied in this paper, the shape of each individual cell is either square or rectangular. Secondly, in order to get high-fidelity numerical results while minimising computational costs, the multi-resolution meshing strategy is used. In detail, the domain is then divided into four separate regions called Domain, Fluid Plane, Transition and Overset. As the mesh is located far from the area of interest, its size increases while its density becomes sparser. Meanwhile, the overset mesh approach is employed to ensure that the meshes around the body boundary can move with the object in a feasible way. The overall arrangement and detailed information of the mesh distribution can be seen in Fig. 3, using the ship section model as a reference. Thirdly, in terms of the specific mesh size in different regions and the boundary layer around the body, we also refer to the corresponding statements in Section 3.1 of Sui et al. (2024), namely it depends on the characteristic height of each body model. However, to prevent a redundant presentation, we will not elaborate on dimensional information of meshes here but only provide the total number of meshes for each body model, as shown in Table 3.

Furthermore, the time step varies with different water exit cases and is always determined by satisfying the Courant-Friedrichs-Lewy (CFL)

 Table 1

 Detailed information on the outlines and dimensions of the body models.

Model	Dimension	Contour	Notes
Wedge	2 m width and 30-deg deadrise angle	2 m	
Ship section	0.034 m width and 0.045 m height	0.034 m	Refer to Aarsnes (1996)

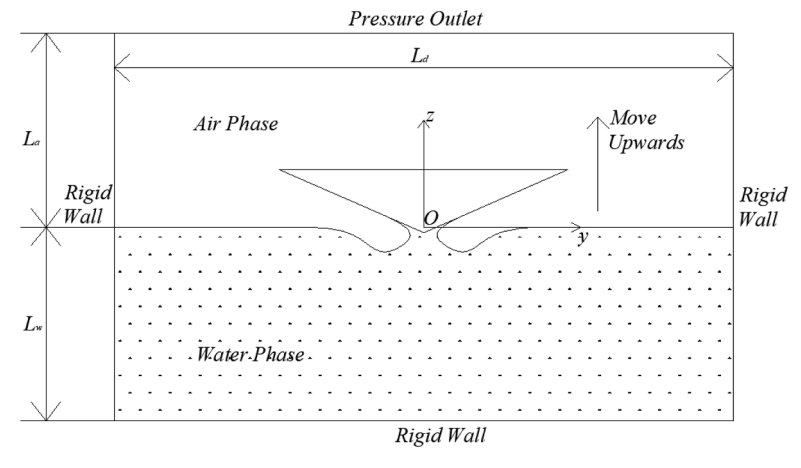


Fig. 2. General sketch of the computational domain for the wedge model.

 Table 2

 Dimensions of the computational domain for each body model.

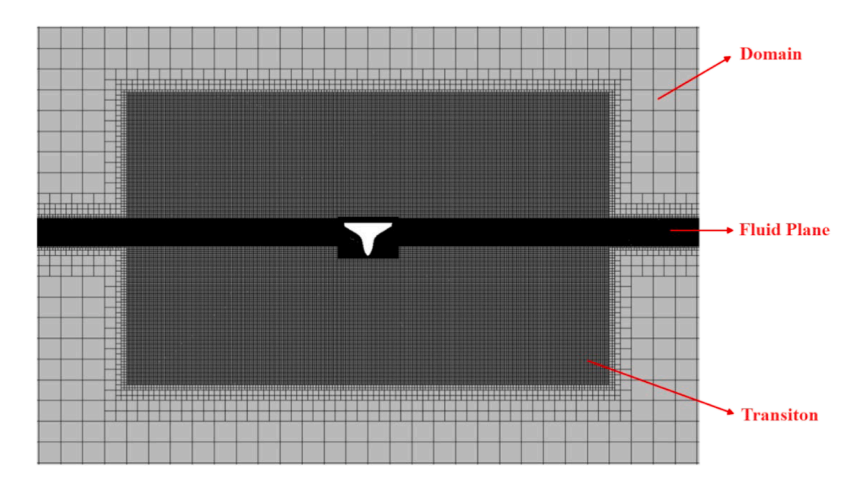
Model	L_d	L_a	L_w
Wedge	30 m	8 m	8 m
Ship section	1.4 m	0.4 m	0.4 m

condition throughout the water exit process. The computer used to run all simulation cases is a Windows-based computer with a Core i5-12500 processor, which has 6 cores and a speed of 3.0 GHz, and 16 GB of RAM. Roughly speaking, the simulation time for each case is 3.3 core hours for the wedge model and 4.2 core hours for the ship section model.

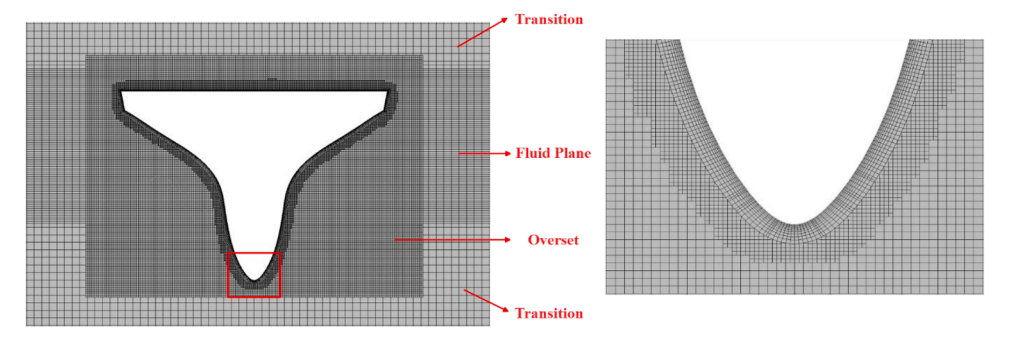
Table 3Total number of meshes for each body model.

Model	Number of meshes		
Wedge	138286		
Ship section	154978		

Subsequently, a test case is introduced to assess the validity and reliability of our numerical configurations. General information related to this test case refers to the work of Korobkin et al. (2017). Specifically, a parabolic model, whose contour can be represented by $z=y^2/2.8$, is used and submerged with an initial immersion height d_0 of 0.01 m.



(a) Overall view



(b) Zoomed views

Fig. 3. Mesh distribution for the ship section model.

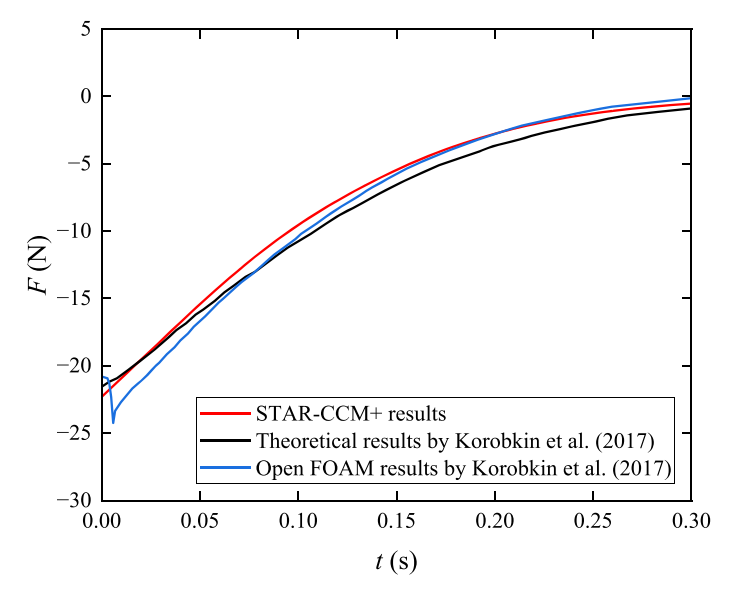


Fig. 4. Verification for the CFD strategy used in this paper.

Afterwards, the body starts moving upwards, given a motion with a prescribed acceleration a=1-2t m/s². The total force acting on the body is computed using the numerical setups mentioned above and then compared with results provided by Korobkin et al. (2017), as shown in Fig. 4. It can be observed from Fig. 4 that our simulation results have a significant agreement with those by Korobkin et al. (2017), whether using the theoretical model or OpenFOAM. Based on the satisfactory performance of numerical setups described in this section, it can be expected that our STAR-CCM+ cases are able to provide high-fidelity results for the water exit problem we investigate in this paper. The same configurations will be used in the following discussion, if not specified.

4. Investigation on the pressure distribution using the POD-ROM method

In this section, the POD-ROM method introduced in this paper is applied to the pressure distribution along the wetted surface of the body. The database is comprised of high-fidelity results from numerical cases simulating various water exit cases, using the setups which have been verified in Section 3. For a comprehensive investigation, each body model in Table 1 is given a few imposed motion cases featured with different initial immersion conditions r_{ic} and constant accelerations a. It should be noted that future applications of the POD-ROM method will not be confined to scenarios with constant acceleration. Some evidence can be found in the work of Sun et al. (2022) and Sui et al. (2024), where 2D water entry and exit problems were studied using the concept of load decomposition. Moreover, in addition to the POD functions included in Eq. (15), the evolution of the wetted length of the body will also be investigated in this section. Detailed information of water exit cases and

Table 4Detailed information on the water exit cases for the wedge model.

Model	Case No.	Immersion condition r_{ic}	Acceleration a
Wedge	1 2	0.953	8 g m/s ² 6 g m/s ²
	3	0.770	$4 g m/s^2$
	4 5	0.779	$8 g m/s^2$ $6 g m/s^2$
	6		$4 g m/s^2$
	7 8	0.606	$8 g m/s^2$ $6 g m/s^2$
	9		4 g m/s ²

subsequent discussions for different body models are presented in the following two subsections.

4.1. Pressure distribution of the wedge model

Firstly, the study of the pressure distribution along the wetted surface of the wedge model using the POD-ROM method is illustrated. The model is given a group of motion cases numbered from 1 to 9, whose details are listed in Table 4. Specifically, the wedge body moves upwards with different constant accelerations a of 8|g|, 6|g| and 4|g| m/s², under different initial immersion conditions r_{ic} of 0.953, 0.779 and 0.606, respectively.

After numerically running each water exit case in STAR-CCM+, pressure distribution snapshots along the wetted surface of the wedge are collected and then constitute the high-fidelity database. Before implementing the POD-ROM method on the pressure field database, the evolution of the wetted half-width of the body is researched, as shown in Fig. 5. Here, an additional parameter $\eta = c/c_0$ is introduced as the nondimensional wetted half-width of the body. Each line or marker symbol in Fig. 5 denotes cases with the same constant acceleration, whereas each colour signifies those with the same initial immersion condition. It can be found from Fig. 5 that the results of η across all cases show a perfect agreement with each other, suggesting that neither the initial immersion condition nor the motion state of the body affects the evolution of η . Moreover, the wetted surface of the wedge diminishes at a rapid rate at the beginning, then the rate slows down and becomes steady during the latter phase of water exit. When the tip point of the wedge is raised to the free surface plane, the wetted width is only about one-fifth of the initial situation. Furthermore, as η is dependent on the non-dimensional displacement ξ , it is also categorised as a temporal function, similar to the time coefficient $a_{p,k}$.

Subsequently, our proposed POD-ROM method is applied to the collected pressure distribution snapshots. All basis modes are obtained by performing the decomposition procedure outlined in Eqs. (5)-(9) and then ordered according to their corresponding eigenvalues. By satisfying Eqs. (12) and (13), the first two modes are identified as the dominant POD basis modes, used for reconstructions and further predictions of the pressure distribution. The energy proportion ω_i of these modes across all water exit cases is shown in Fig. 6. It is noted that each figure is divided into three areas reflecting different initial immersion conditions, with bars of the same colour denoting the specific constant acceleration. It can be clearly observed from Fig. 6 that the 1st POD basis modes account

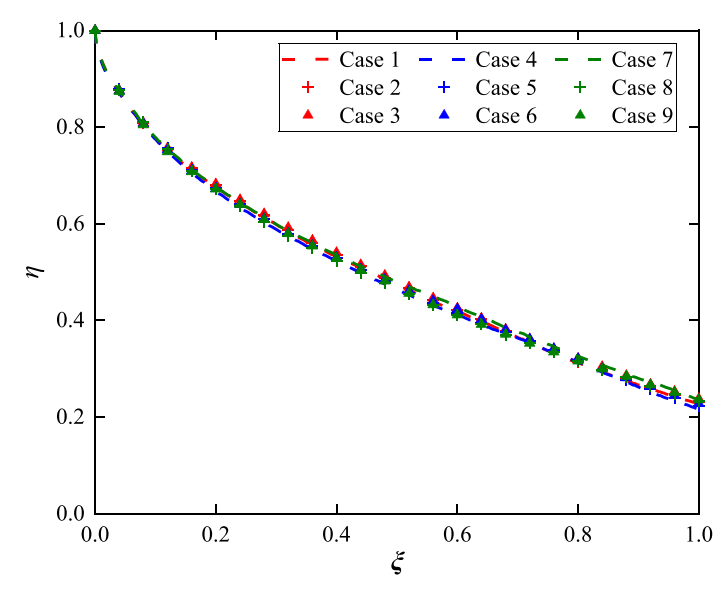


Fig. 5. Evolution of the non-dimensional wetted half-width η for the wedge model. (Each line or marker symbol denotes cases with the same constant acceleration, whereas each colour signifies cases with the same initial immersion condition.).

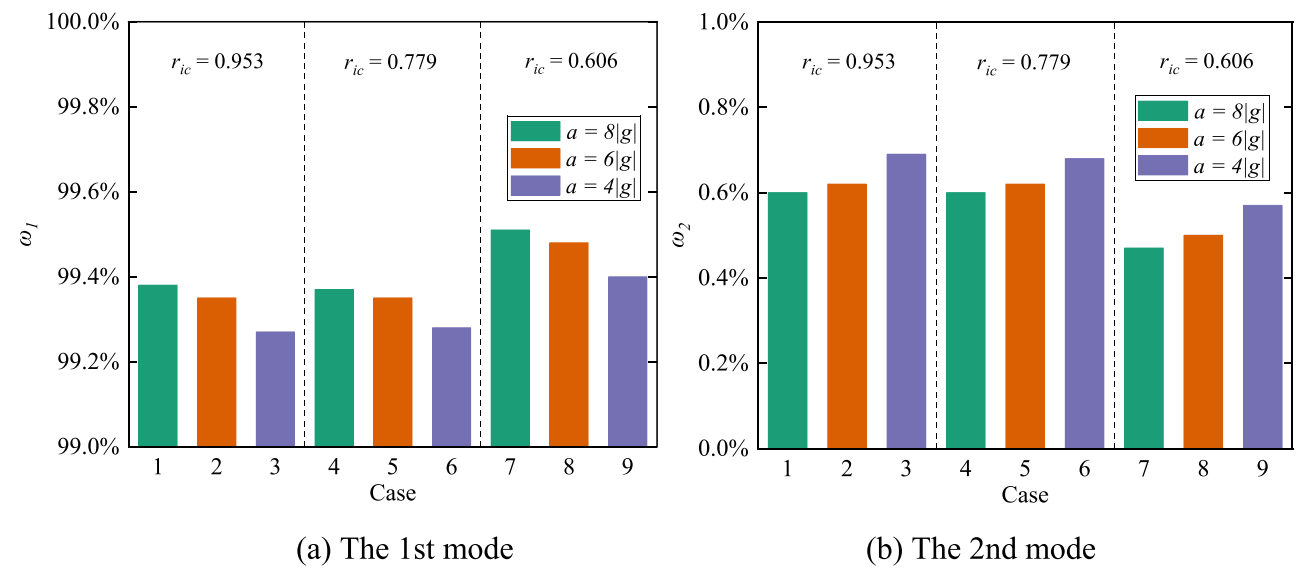


Fig. 6. Energy proportion ω_i of the POD basis modes for the wedge model. (Each figure is divided into three areas reflecting different initial immersion conditions, with bars of the same colour denoting the specific constant acceleration.).

for over 99% of the total energy of the system and have an overwhelming influence compared to other modes. In addition, upon specifying the initial immersion condition r_{ic} , the energy proportion of the 1st basis mode exhibits a slight decline while that of the 2nd basis mode tends to increase, as the amplitude of the constant acceleration decreases. Although it will not lead to a significant impact on the pressure distribution reconstruction, this finding suggests that nonlinear effects are rising when the amplitude of body acceleration approaches that of velocity. Additionally, the 2nd basis mode seems to contribute little to the pressure distribution reconstruction, nonetheless it should not be assumed that these modes are classified as weak modes. Some evidence and discussions can be found in Section 5.

Following the identification of two dominant POD basis modes, their modal profiles and associated time coefficients for all water exit cases are shown in Figs. 7 and 8, respectively. Moreover, profiles of the mean mode are shown in Fig. 9. Some interesting findings can be made from these figures. Firstly, all POD functions are almost independent of both

the initial immersion condition and the motion state of the body, which is the same as η . This can be explained by considering the analytical formula of $P_A(\sigma,\xi)$, namely Eq. (4). More specifically, based on the wedge-shaped model discussed here, we have $\zeta=\tan 30^{\circ}\sigma$ and $d_0=\tan 30^{\circ}c_0$. In this case, Eq. (4) can be further written as:

$$P_{A} = \frac{-\sqrt{c^{2} - (c\sigma)^{2} - \tan 30^{\circ} c\sigma + \tan 30^{\circ} c}}{\tan 30^{\circ} c_{0}}$$

$$= \frac{c}{c_{0}} \left(-\frac{\sqrt{1 - \sigma^{2}}}{\tan 30^{\circ}} - \sigma + 1 \right)$$

$$= \eta \left(-\frac{\sqrt{1 - \sigma^{2}}}{\tan 30^{\circ}} - \sigma + 1 \right)$$
(16)

According to the analytical expression of Eq. (16) and the results from the evolution of η (namely Fig. 5), there is no component in Eq. (16) associated with the initial immersion condition or the motion state

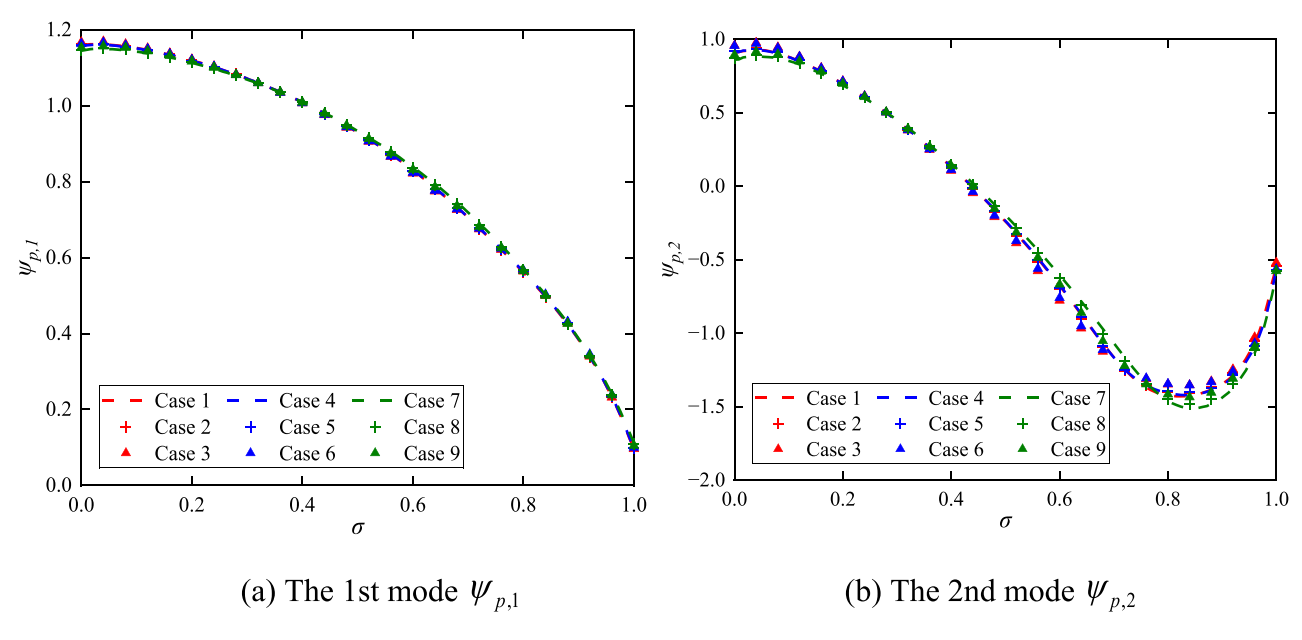


Fig. 7. Non-dimensional POD basis modes $\psi_{p,k}$ for the wedge model. (Each line or marker symbol denotes cases with the same constant acceleration, whereas each colour signifies cases with the same initial immersion condition.).

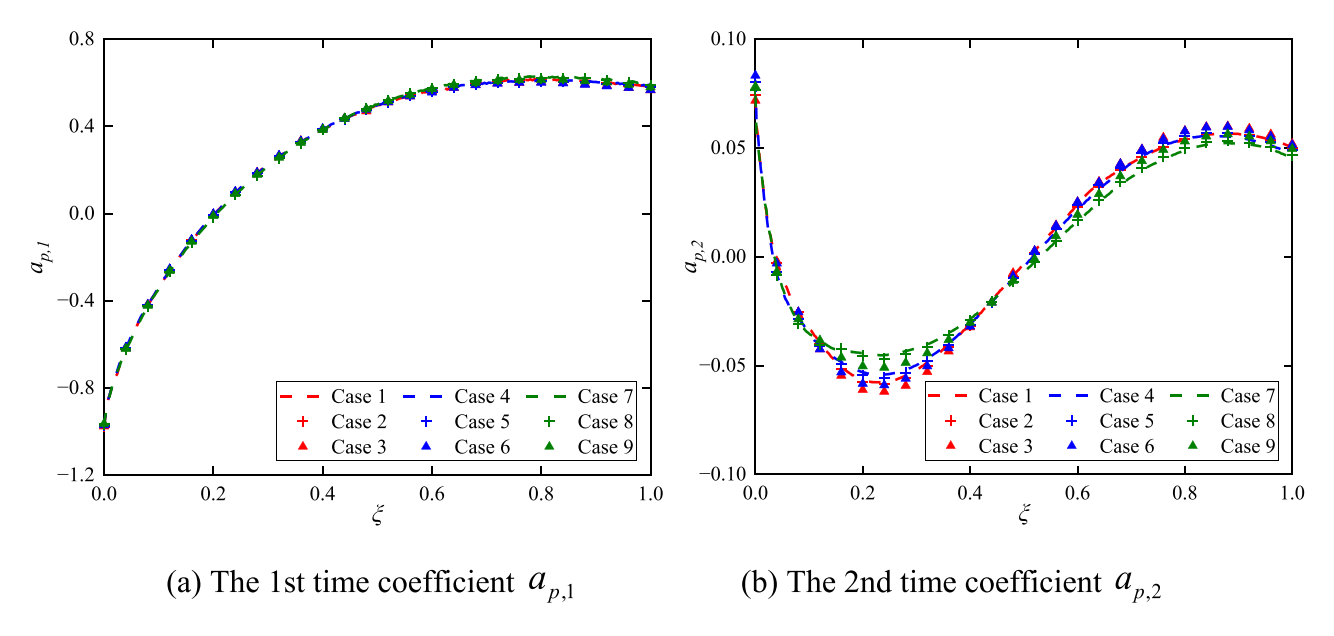


Fig. 8. Non-dimensional time coefficient $a_{p,k}$ for the wedge model. (Each line or marker symbol denotes cases with the same constant acceleration, whereas each colour signifies cases with the same initial immersion condition.).

of the body. Therefore, it is not surprising that each POD function shown in Figs. 7-9 exhibits a perfect match with each other across all water exit cases. Relevant evidence can also be found in the work of Sui et al. (2024), where it was concluded that the total force acting on a body directly lifting out of the water depends only on the body displacement.

Furthermore, let us pay attention to the detailed profiles of different POD functions. In terms of the 1st POD basis mode depicted in Fig. 7(a), the modal amplitude shows a negative correlation with the distance from the tip point. In accordance with its time coefficient plotted in Fig. 8(a), this mode initially provides the body with pulling loads but changes to lifting loads at around $\xi=0.25$. In contrast, the 2nd basis mode presented in Fig. 7(b) has a more complicated profile than the 1st one. Simultaneously, based on its associated time coefficient in Fig. 8(b), this mode provides negative loads to the body wetted area of $\sigma \in [0,0.4]$ and positive loads to the area of $\sigma \in [0.4,1]$ during the early phase of

water exit. However, the circumstances are completely reversed during the latter phase. Considering that these two POD basis modes have comparable modal amplitudes but significant differences exist in their corresponding time coefficients (refer to Fig. 8), it is undoubtable that the 1st basis mode contains most of the energy inside the entire hydrodynamic system. In terms of the mean mode shown in Fig. 9, the location with the maximum average pressure is at around $\sigma=0.4$, instead of at the tip point. This finding contradicts the linear theoretical model by subtracting $p_{non-linear}$ from Eq. (2), indicating that nonlinear effects tend to provide positive loads to the body and become stronger as the location approaches the bottom.

From our point of view, similar results can be anticipated for any wedge-shaped model. Upon defining the wedge size, all POD functions and the evolution of the wetted half-width are determined correspondingly. In this case, after deriving them from a single CFD simulation, the

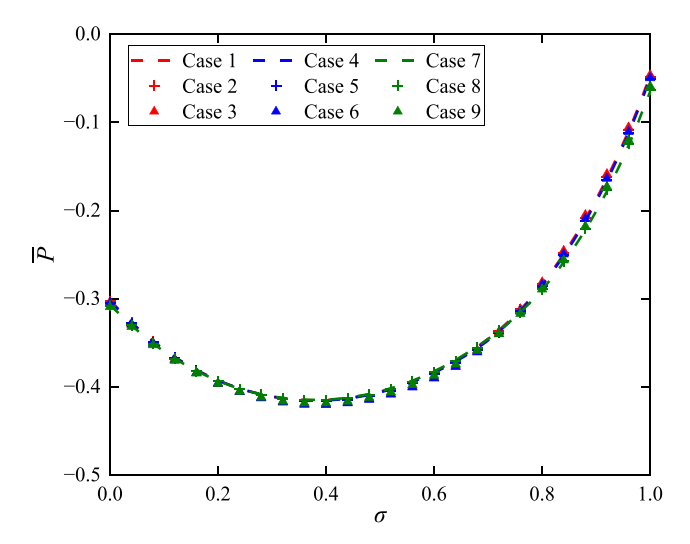


Fig. 9. Non-dimensional mean mode \overline{P} for the wedge model. (Each line or marker symbol denotes cases with the same constant acceleration, whereas each colour signifies cases with the same initial immersion condition.).

pressure distribution along the body wetted surface under any further water exit case can be rapidly evaluated using Eq. (15), instead of repeating the same numerical configurations. It can be expected that computational resources can be saved a lot by using the POD-ROM method proposed in our paper. In light of the motivational findings, the application of the POD-ROM method to the model with a more complex contour, namely the ship section model, will be examined in the next subsection.

4.2. Pressure distribution of the ship section model

In this subsection, the pressure distribution of the practical ship section model is discussed using the POD-ROM method. A total of fifteen different water exit cases, numbered from 10 to 24, are given to this model, as listed in Table 5. It should be noted that constant accelerations a of 8|g|, 6|g| and 4|g| m/s² are still used here, while five different initial immersion conditions r_{ic} of 1, 0.889, 0.778, 0.667 and 0.556 are examined to evaluate the impact of the body submerged depth at the first instant.

Following the same procedure conducted for the wedge model, a high-fidelity database of pressure distribution information is firstly constructed upon completion of all numerical simulations using STAR-CCM+. The evolutions of the non-dimensional wetted half-width η under different water exit cases are described in Fig. 10. It is clear to see that, in contrast to the findings for the wedge model, the initial

Table 5Detailed information on the water exit cases for the ship section model.

Model	Case No.	Immersion condition r_{ic} Accelerat	
Ship section	10	1 $8 g m/s^2$	
	11		$6 g m/s^2$
	12		$4 g m/s^2$
	13	0.889	$8 g m/s^2$
	14		$6 g m/s^2$
	15		$4 g m/s^2$
	16	0.778	$8 g m/s^2$
	17		$6 g m/s^2$
	18		$4 g m/s^2$
	19	0.667	$8 g m/s^2$
	20		$6 g m/s^2$
	21		$4 g m/s^2$
	22	0.556	$8 g m/s^2$
	23		$6 g m/s^2$
	24		$4 g m/s^2$

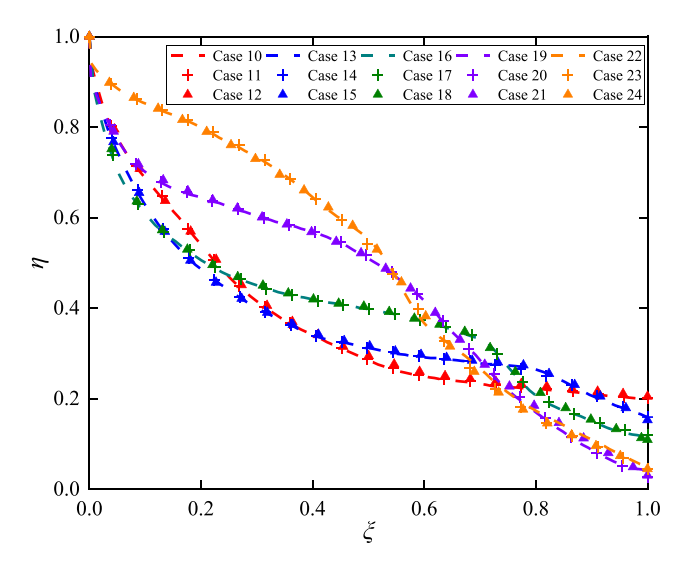


Fig. 10. Evolution of the non-dimensional wetted half-width η for the ship section model. (Each line or marker symbol denotes cases with the same constant acceleration, whereas each colour signifies cases with the same initial immersion condition.).

immersion condition r_{ic} has a significant influence on the wetted surface of the ship section model. From our point of view, it is the body contour of the ship section model, which is more complicated than the wedge-shaped model, that accounts for this discrepancy. Unfortunately, based on the available models proposed by Korobkin (2013) and Korobkin et al. (2017), it seems to be quite challenging to conduct an in-depth investigation on the variation of the body's wetted surface using theoretical methods. However, it is still an inspiring discovery that the development of $\mathfrak n$ is not affected by the motion state of the body.

The POD-ROM method is then applied to the pressure field snapshots. In terms of identifying the dominant POD basis modes, it is expected that more basis modes will be included compared to the wedge model, owing to the more complex geometry of the ship section model and the associated stronger nonlinear factors. In fact, in order to both appropriately represent the dynamic characteristics of the pressure distribution and satisfy Eqs. (12) and (13), just one more basis mode has to be included, indicating that the dominant POD basis mode group for this ship section model has three modes in total. The energy proportions of these three modes across all water exit cases are shown in Fig. 11. The regulations for the division of the figures and the colour-filling of the bars follow the example of the wedge model. It can be easily seen from Fig. 11(a) and (b) that the 1st basis mode contains less energy compared to that of the wedge model, while the 2nd basis mode increasingly becomes essential as the initial immersion height d_0 increases. For instance, when the model is given an initial immersion condition r_{ic} of 0.556, the 1st basis mode accounts for about 95% of the total energy of the system, but the ratio drops steeply to around 80% under the case of $r_{ic} = 0.889$. Simultaneously, a difference of about 10% in the energy that the 2nd basis mode contains can be found between these two cases. However, it is beyond our expectation that the energy proportion of the 1st basis mode rises when the initial immersion condition r_{ic} grows from 0.889 to 1. From our understanding, this phenomenon can be explained by the fact that the dimensional contour of the ship section appears almost linear at this height range, hence enhancing the linearity of the system. Detailed information on the submerged contour of the ship section model under different immersion conditions is shown in Fig. 12.

Concerning the general profiles of POD functions, Figs. 13 and 14 present those of all dominant POD basis modes and their corresponding time coefficients across all water exit cases, followed by Fig. 15 depicting those of the mean mode. It can be observed from these figures that all POD functions are affected by the initial immersion condition

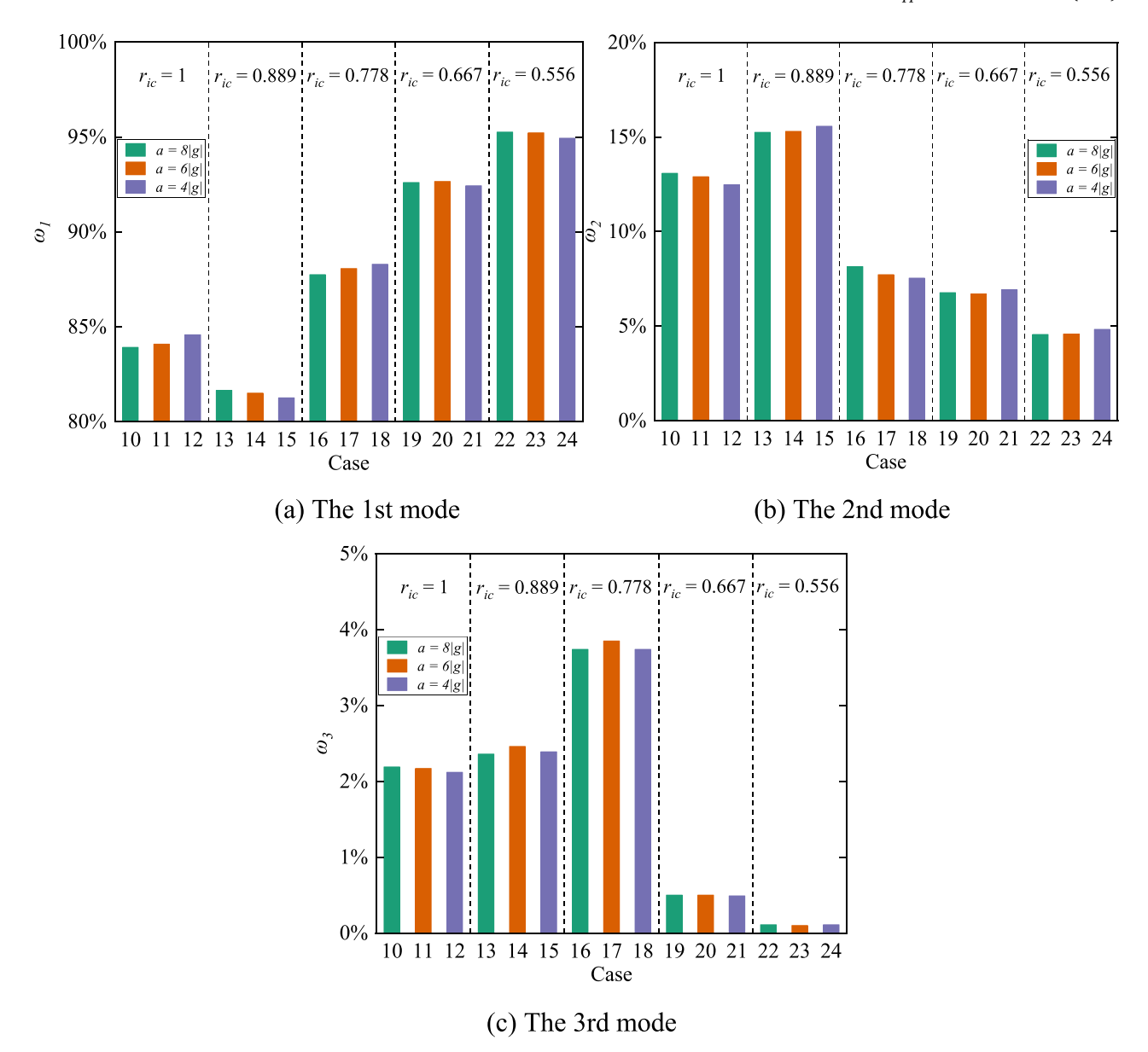


Fig. 11. Energy proportion ω_i of the POD basis modes for the ship section model. (Each figure is divided into three areas reflecting different initial immersion conditions, with bars of the same colour denoting the specific constant acceleration.).

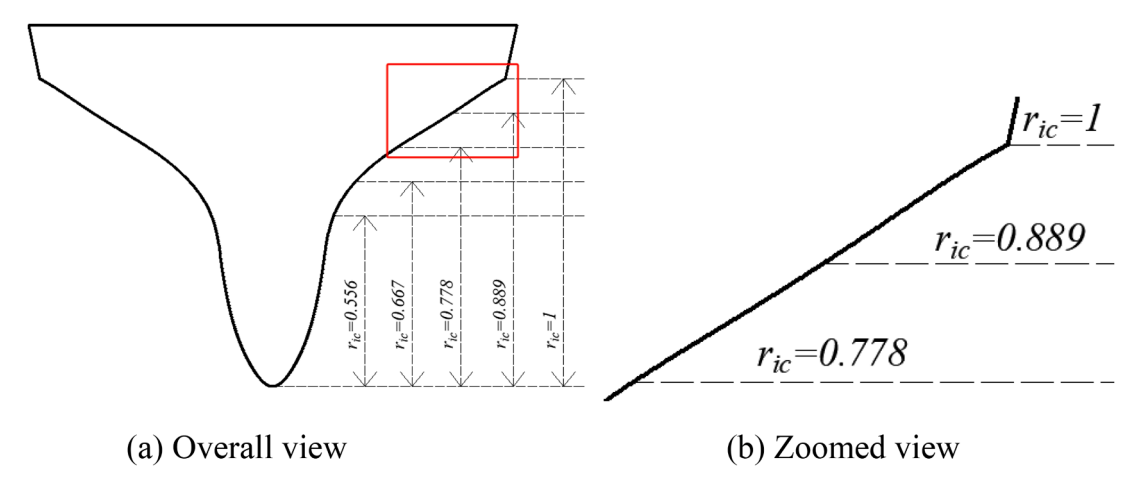


Fig. 12. Submerged contour of the ship section model under different immersion conditions.

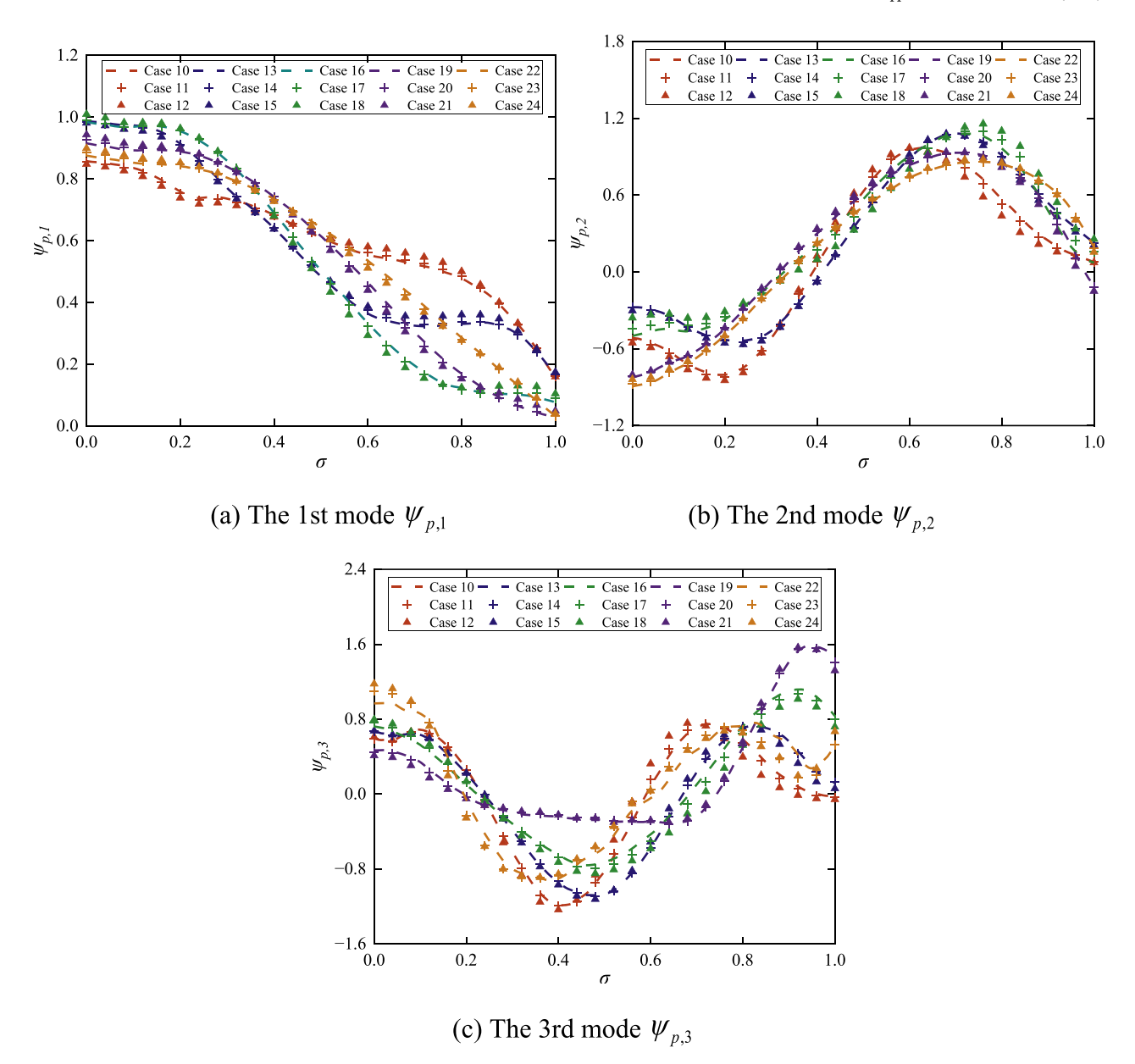


Fig. 13. Non-dimensional POD basis modes $\psi_{p,k}$ for the ship section model. (Each line or marker symbol denotes cases with the same constant acceleration, whereas each colour signifies cases with the same initial immersion condition.).

but remain independent of the motion state of the body, which is consistent with the findings from the evolution of the body wetted surface. Continuing to refer to the analytical formula of $P_A(\sigma, \xi)$ (namely Eq. (4)) for clarification, we can no longer derive the straightforward equation as shown in Eq. (16), due to the complex body contour of the ship section model. Additional supporting evidence can also be found in the work by Sui et al. (2024), who confirmed that the immersion state has a considerable effect on the hydrodynamic force acting on the body. However, using the POD-ROM method, it can be noticed that, in comparison to the temporal functions (namely the evolution of the wetted half-width η (Fig. 10) and the time coefficient $a_{p,k}$ (Fig. 14)), the spatial functions (namely the POD basis modes $\psi_{p,k}$ (Fig. 13) and the mean mode \overline{P} (Fig. 15)) appear to suffer less from the variation in the initial immersion condition. In other words, although there is no considerable agreement in each spatial function between different water exit cases, the overall distribution throughout the spatial domain stays consistent.

Moreover, paying attention to the detailed profiles of the mean mode (namely Fig. 15), the maximum average pressure occurs at locations

around $\sigma \in (0.5, 0.7)$. Meanwhile, the region close to the keel experiences negligible average pressure, which reflects on the strong nonlinear factors. It is also interesting to find some regularities in the evolutions of certain time coefficients. Using the 1st time coefficient plotted in Fig. 14 (a) as an example, the trend of variation seems to follow a specific pattern: first it rises steadily to a peak, then falls sharply and finally stabilises at a nearly constant level. Unique evolution regularities existing in the other two time coefficients, as well as the body's wetted half-width shown in Fig.10, can also be identified in a similar manner. In the aforementioned context, the development of the flow around the body boundary is expected to adhere to a certain pattern determined by the body dimensions. In other words, each temporal POD function has its own characteristic evolution pattern, with the initial immersion condition playing the role of identifying the exact evolution stage and rate. This is a remarkably inspiring finding, as it obviates the necessity to derive all POD functions for each potential initial immersion condition, thereby greatly facilitating the prediction of pressure distribution along the wetted surface of the body. Consequently, our proposed POD-ROM

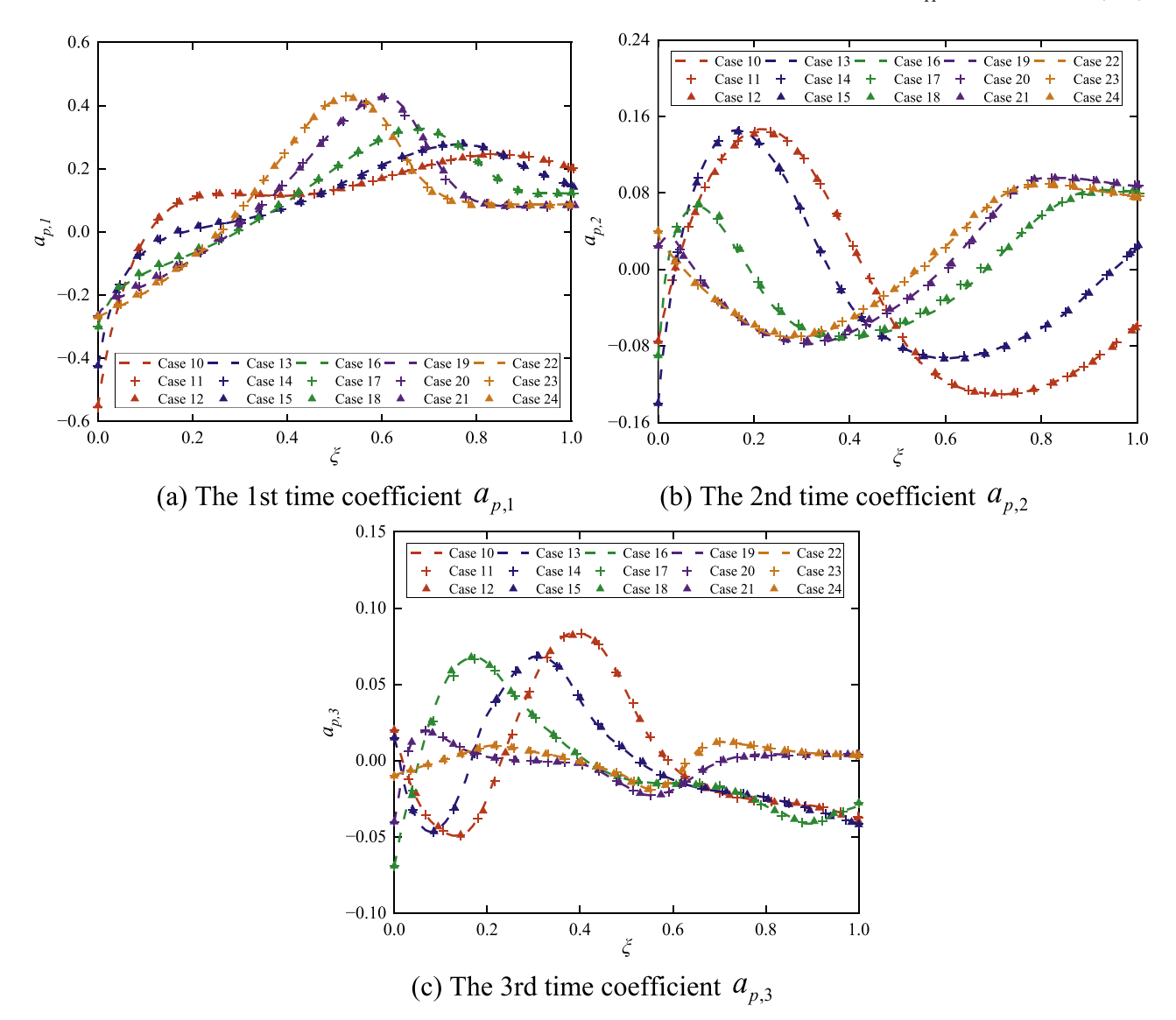


Fig. 14. Non-dimensional time coefficient $a_{p,k}$ for the ship section model. (Each line or marker symbol denotes cases with the same constant acceleration, whereas each colour signifies cases with the same initial immersion condition.).

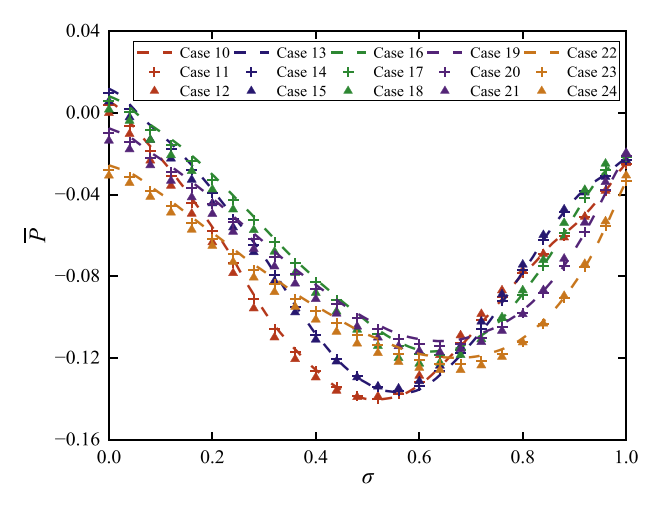


Fig. 15. Non-dimensional mean mode \overline{P} for the ship section model. (Each line or marker symbol denotes cases with the same constant acceleration, whereas each colour signifies cases with the same initial immersion condition.).

method can be developed for application in more intricate water exit cases, particularly those relevant to real maritime engineering. Further discussions on the characteristic evolution pattern can be found in Section 5.2, following the evaluation of the accuracy of pressure distribution predictions using the POD-ROM method.

5. Verification of the POD-ROM method and further discussions

From our findings in the last section, a complicated water exit problem of full dimensions can be approximated by an equivalent one represented by only two POD basis modes for the wedge model, while three POD basis modes for the ship section model. This order reduction significantly benefits the study on the dynamic variation of the pressure distribution along the wetted surface of the body, with not only preserving crucial features but also saving a lot of computational time. In order to assess the validity and reliability of the POD-ROM method, the predictions of pressure distribution along the wetted surface of the body will be examined in this section. Afterwards, the so-called characteristic evolution pattern for each temporal POD function of the ship section model will be explored and discussed. More details can be found in the following two subsections.

5.1. Verification of the POD-ROM method

The validity and reliability of the POD-ROM method are evaluated by providing each body model investigated in this paper with a test water exit case and then comparing the predicted pressure distribution with numerical results by STAR-CCM+. Detailed information on these two test cases is listed in Table 6. The wedge model is given a case with an initial immersion condition and a constant acceleration, neither of which were researched in prior studies. In contrast, the ship section model is given a case where the initial immersion condition has already been explored in Section 4.2 and only the constant acceleration is changed, considering the substantial impact of the initial immersion condition on its temporal POD functions. All POD functions for both test cases used to predict the pressure distribution do not need derivation from supplementary STAR-CCM+ simulations, because they are available in the results presented in Section 4. Specifically, any individual profile in each graph from Figs. 7-9 is applicable to the wedge model, while the blue profiles in each graph from Figs. 13-15 can be used for the ship section model. Moreover, in order to have a quantitative error analysis to examine the accuracy of predictions provided by the POD-ROM method, the root mean squared error (RMSE) is calculated, which can be defined as:

$$RMSE = \sqrt{\frac{1}{N} \sum_{i=1}^{N} \left(\widehat{p}_{pre}(y_i) - \widehat{p}_{cfd}(y_i) \right)^2}$$
 (17)

where \widehat{p} is the non-dimensional pressure and expressed as $\widehat{p}=p$ $/\left(0.5\rho\overline{v}^2\right)$ where ρ means the fluid density and \overline{v} denotes the average speed of the body; \widehat{p}_{pre} and \widehat{p}_{cfd} are predicted and CFD results of the non-dimensional pressure, respectively; N is the amount of data for analysis. In this paper, the pressures of a group of discrete locations with an interval of $\Delta\sigma=0.008$ take part in the quantitative error analysis, indicating that N is equal to 126.

The predicted pressure distribution along the wetted surface of the wedge model is first shown in Fig. 16, compared with the simulation results obtained from STAR-CCM+. Four different instants during the whole water exit process are investigated, namely when the non-dimensional displacement of the body ξ is 0.2, 0.4, 0.6 and 0.8, respectively. To demonstrate the importance of the 2nd basis mode for accurate predictions, results using just one POD basis mode are also shown. It can be seen from Fig. 16 that the predictions using two POD basis modes are in satisfactory agreement with those from numerical simulations. Even if the 1st basis mode accounts for almost 99% of the total energy of the system, using just one basis mode fails to provide predictions with sufficient precision. In addition, RMSE is calculated to further demonstrate the accuracy of predicted pressure distributions using two POD basis modes, as listed in Table 7, where all RMSE values are below 0.1209.

With regard to the pressure distribution predictions for the ship section model, the results corresponding to ξ of 0.2, 0.4, 0.6 and 0.8 are shown in Fig. 17. It can be observed that, comparing the results using two and three POD basis modes, the 3rd basis mode contributes greatly to the precise representation of pressure distribution, in terms of both amplitude and spatial profile. Although the energy that the 3rd basis mode contains accounts for only around 4% of the whole system, the necessity to identify three dominant POD basis modes is validated. RMSE is also computed here to conduct a quantitative error analysis on the predictions using three POD basis modes, as shown in Table 8, where

 Table 6

 Detailed information on the test water exit cases for different body models.

Model	Case No.	Immersion condition r_{ic}	Acceleration a
Wedge	25	0.85	3 g m/s ²
Ship section	26	0.889	9 g m/s ²

all RMSE values are below 0.0734.

In light of the inspiring agreements shown in Figs. 16 and 17, it can be concluded that our proposed POD-ROM method is able to provide the predictions of the pressure distribution along the body wetted surface in an effective and efficient way. In the meantime, if both body size and initial immersion conditions are specified, future predictions with a certain degree of accuracy can also be achieved using pre-obtained POD functions from a single CFD simulation, thereby conserving computational resources by avoiding redundant theoretical calculations or numerical setups.

5.2. Further discussions on characteristic evolution patterns of the ship section model

As stated in Section 4.2, the temporal POD functions of the ship section model, namely the time coefficient $a_{p,k}$ and the evolution of the wetted half-width η , are greatly influenced by the initial immersion condition. It indicates that repeating CFD simulations are necessary to derive all POD functions for each given case of the initial immersion condition, limiting the practical application of our proposed POD-ROM method. However, after noticing certain regularities in the variation trend of these functions, this issue can be addressed by identifying their own characteristic evolution patterns. Therefore, this subsection is aimed at exploring the patterns for each temporal POD function of the ship section model.

From our viewpoint, these characteristic evolution patterns can be determined by the particular water exit case in which the ship section model is first submerged with the deepest initial immersion condition r_{ic} of 1 and then moves upwards until the non-dimensional wetted halfwidth η reaches zero. It should be noted that, in this case, the scope of the non-dimensional displacement of the body ξ would be expanded. According to our high-fidelity simulation results, the whole body surface becomes completely dry at around $\xi=2$.

Subsequent manual scaling and translation adjustments in both lateral and vertical dimensions are made to the original graphs of each temporal POD function shown in Figs. 10 and 14, until the postadjustment graphs match the characteristic evolution patterns as closely as possible. In fact, a similar strategy has been used in the work by Sui et al. (2024), who also identified certain regularities in terms of the force development of the same ship section model. It has been proved in their paper that the so-called characteristic evolution pattern does exist. Focusing on our study, assuming that our supposition has been validated by the aforementioned manual adjustments, the reverse treatment is essential for further predictions, considering any given initial immersion condition $r_{ic} = r_{ica}$. In this case, a group of empirical formulae is summarised as Eqs. (18)-(22):

$$\eta' = \varepsilon_0 \eta \tag{18}$$

$$a'_{p,1} = \varepsilon_1 a_{p,1} + \varepsilon_2 \tag{19}$$

$$a'_{p,2} = \varepsilon_3 a_{p,2} + \varepsilon_4 \tag{20}$$

$$a'_{p,3} = \varepsilon_5 a_{p,3} + \varepsilon_6 \tag{21}$$

$$\xi = \mu \xi + \begin{cases} \varepsilon_7 & \text{when focusing on } \eta \\ \varepsilon_8 & \text{when focusing on } a_{p,1} \\ \varepsilon_9 & \text{when focusing on } a_{p,2} \\ \varepsilon_{10} & \text{when focusing on } a_{p,3} \end{cases}$$
(22)

where the variables denoted by the superscript " '", named as the characteristic variables, reflect the corresponding values within the characteristic evolution patterns associated with different temporal POD functions; ε_0 - ε_{10} and μ are different parameters whose formulae are shown as Eqs. (23)-(34):

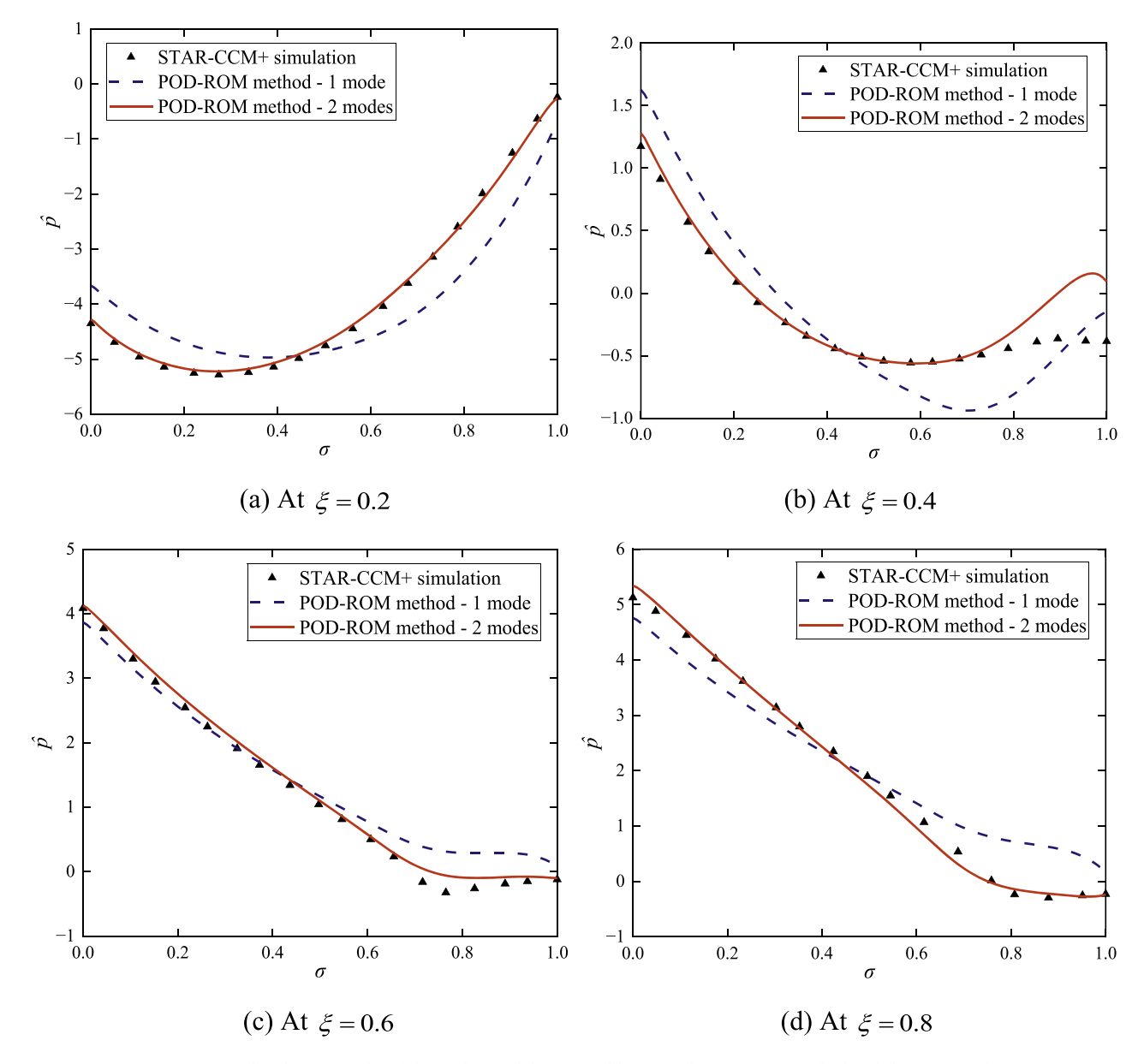


Fig. 16. Pressure distribution results of the wedge model compared between the POD-ROM method and the CFD simulation.

Table 7RMSE on the pressure distribution of the wedge model.

Displacement ξ	0.2	0.4	0.6	0.8
RMSE	0.0697	0.1826	0.1201	0.1209

$$\varepsilon_0 = \frac{0.2174r_{ica}}{r_{ica}^3 - 1.709r_{ica}^2 + 0.3520r_{ica} + 0.5744}$$
 (23)

$$\varepsilon_1 = 0.824 r_{ica}^{7.268} + 0.176 \tag{24}$$

$$\varepsilon_2 = -1.644r_{ica}^{7.630} + 1.644 \tag{25}$$

$$\varepsilon_3 = -0.357 r_{ic\alpha}^{5.312} + 1.357 \tag{26}$$

$$\varepsilon_4 = 0.428 r_{ica}^{9.080} - 0.428 \tag{27}$$

$$\varepsilon_5 = -0.565 r_{ica}^{3.839} + 1.565 \tag{28}$$

$$\varepsilon_6 = -2.228r_{ica}^2 + 4.442r_{ica} - 2.214 \tag{29}$$

$$\varepsilon_7 = -1.080 r_{ica} + 1.080 \tag{30}$$

$$\varepsilon_8 = -0.058r_{ica}^2 - 0.459r_{ica} + 0.517 \tag{31}$$

$$\varepsilon_9 = \begin{cases} -0.662 r_{ica}^{5.882} + 0.431, \ 0 \le r_{ica} \le 7/9\\ 0.031 r_{ica}^{-9.229} - 0.031, \ 7/9 \le r_{ica} \le 1 \end{cases}$$
(32)

$$\varepsilon_{10} = \begin{cases} -29.600 r_{ic\alpha}^{17.880} + 0.521, & 0 \le r_{ic\alpha} \le 7/9 \\ -17.010 r_{ic\alpha}^{3} + 47.390 r_{ic\alpha}^{2} - 44.570 r_{ic\alpha} + 14.190, & 7/9 \le r_{ic\alpha} \le 1 \end{cases}$$
(33)

$$\mu = -0.171r_{ica}^{3.198} + 1.171 \tag{34}$$

According to our understanding, the parameters ε_7 - ε_{10} and μ represent the adjustments applied to the lateral dimension, which determine the stage within the characteristic evolution pattern and the evolution rate, respectively. In this case, it is inspiring to find that all

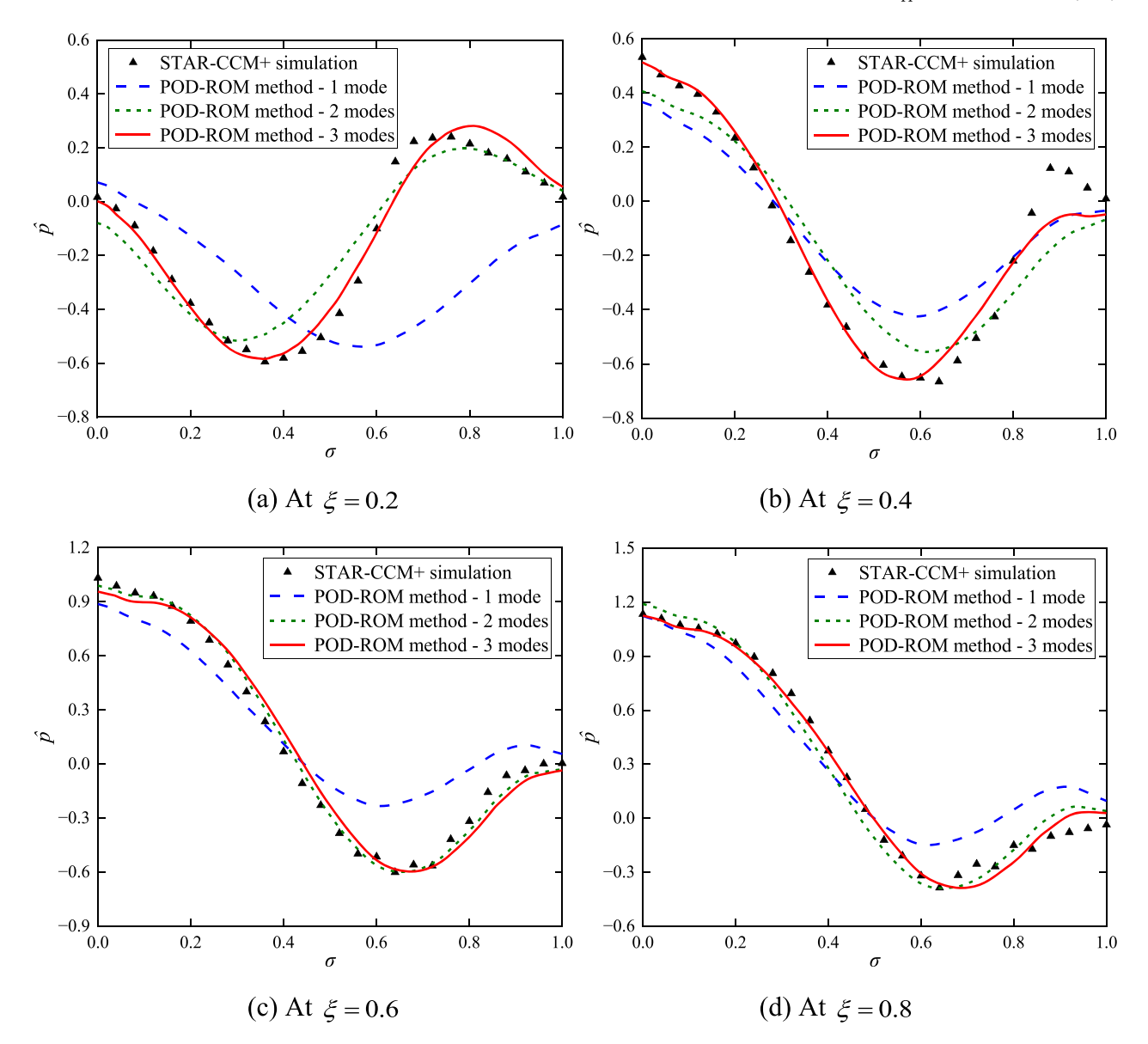


Fig. 17. Pressure distribution results of the ship section model compared between the POD-ROM method and CFD simulation.

Table 8RMSE on the pressure distribution of the ship section model.

Displacement ξ	0.2	0.4	0.6	0.8
RMSE	0.0526	0.0729	0.0734	0.0500

temporal POD functions exhibit a uniform rate under the specified immersion condition $r_{ic} = r_{ica}$, with the rate increasing as the ship section model has a shallower initial immersion depth.

In accordance with Eqs. (18)-(22), the graphs of different temporal POD functions presented in Section 4.2 are respectively adjusted and displayed alongside the characteristic evolution patterns obtained from the case of $r_{ic}=1$ and $\xi\in[0,2]$, which are shown in Fig. 18. It can be seen from Fig. 18 that the post-adjustment profiles of each temporal POD function have a significant agreement with the characteristic evolution patterns (shown by the red lines). Some discrepancies are evident in the initial phase of most adjusted graphs, especially for the functions of $a_{p,2}$ and $a_{p,3}$, but subsequent evolution trends almost correspond to the characteristic pattern and we have attained the optimal match.

In addition, in order to make the existence of the characteristic

evolution pattern and our proposed empirical approach more convincing, further evidence related to the flow around the body boundary is provided in Fig. 19. Specifically, the profiles of the free surface around the ship section at five different characteristic displacements ξ' of 0.6, 0.7, 0.8, 0.9 and 1 are directly extracted from STAR-CCM+ simulations. It can be seen from Fig. 19 that, when the characteristic displacement ξ' is specified, the profiles of the free surface under different initial immersion conditions represent considerable similarity. It is also expected that these profiles can almost achieve a significant agreement after the similar manual scaling and translation adjustments as those used for the temporal POD functions.

Moreover, to assess the validity of our proposed empirical approach, the ship section model is provided with another complicated water exit case where the body acceleration is variable and the initial immersion condition is not studied in our prior investigation. Detailed information related to this water exit case is given in Table 9.

Once the initial immersion condition r_{ic} is specified, the corresponding graphs for each temporal POD function can be obtained using our proposed empirical formulae, namely Eqs. (18)-(34). Afterwards, the pressure distribution along the wetted surface of the ship section model can be easily predicted by directly using spatial POD functions

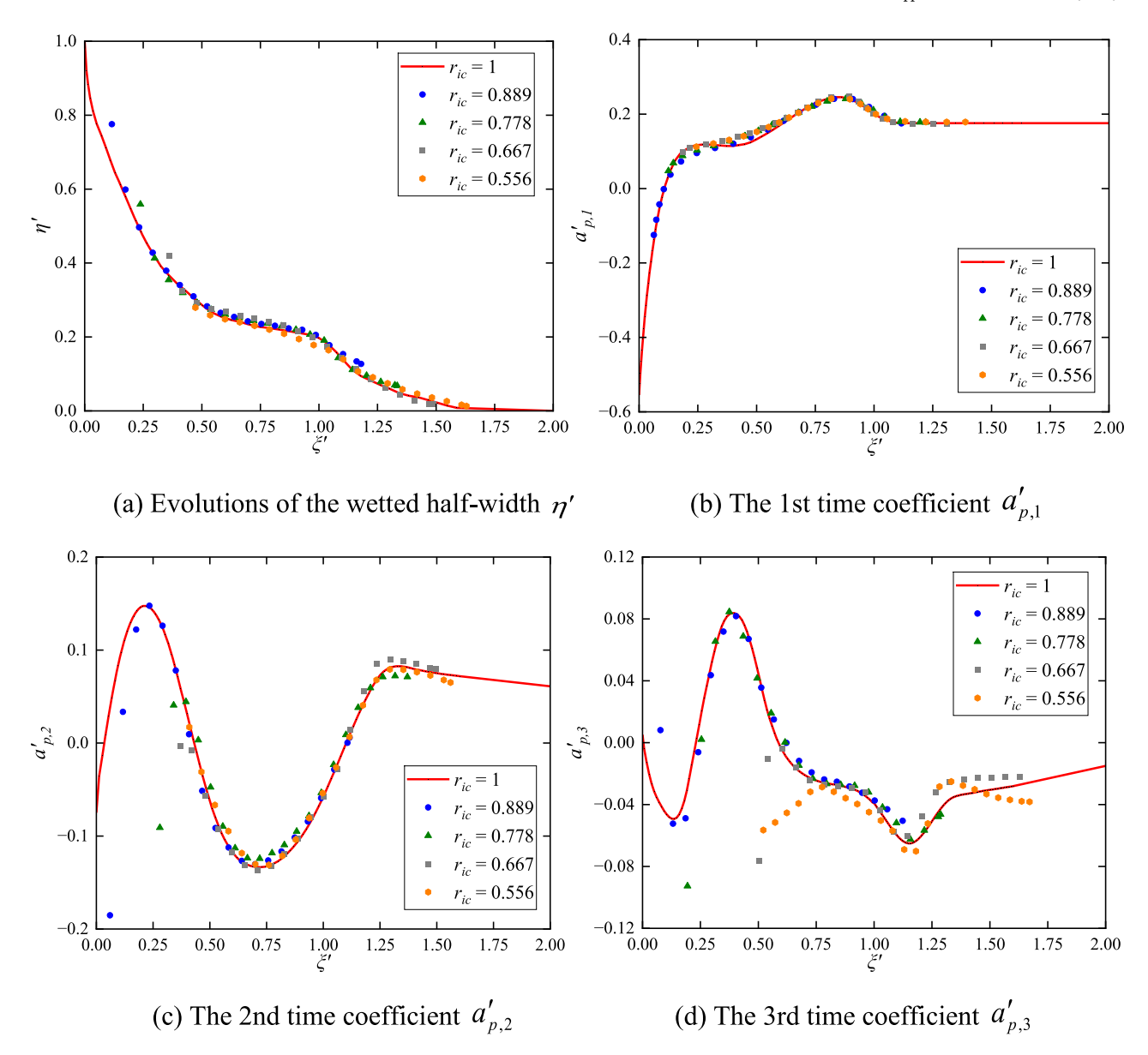


Fig. 18. Temporal POD functions of the ship section model after manual adjustments as Eqs. (18)-(34).

shown in Figs. 13 and 15 and the POD-ROM method introduced in this paper. Here, the pressure distribution profiles at the moments of $\xi = 0.2$. 0.4, 0.6 and 0.8 are compared with the results from STAR-CCM+ simulations, as seen in Fig. 20. A promising finding from these comparisons is that our predictions exhibit a certain degree of accuracy, despite visible underestimations near the keel. The partial mismatch between the adjusted graphs of time coefficients $a_{p,2}$ and $a_{p,3}$ and their respective characteristic evolution patterns may account for these discrepancies. RMSE of the pressure distribution comparisons is presented in Table 10, with all values remaining below 0.179. Meanwhile, a comparison of the development of the wetted half-width is also conducted and shown in Fig. 21, where a significant agreement can be observed, except during the beginning period. Nevertheless, our supposition regarding the characteristic evolution pattern is confirmed by the satisfactory verifications presented in this subsection, and our proposed POD-ROM method has been demonstrated to be applicable to practical and unseen water exit circumstances, not limited to the case with the constant acceleration. Further refinements on the empirical formulae are expected for more accurate predictions.

Furthermore, it is worth mentioning that, although our supposition is

verified only by the ship section model studied in this paper, similar characteristic evolution patterns and associated empirical equations for any model with a complex contour are expected to be obtained by following the procedure outlined in this subsection. In this case, there is no doubt that the prediction of hydrodynamic loads acting on the body can be further facilitated, using related POD functions by numerically running a single water exit case under the deepest immersion condition. Consequently, not only are the redundant theoretical calculations or numerical simulations avoided, but also problems in real maritime engineering can be easily solved.

6. Conclusion

In this paper, the POD-ROM method, combining the concepts of snapshot POD and ROM, is proposed to investigate the 2D water exit problem, where rigid and symmetric bodies are submerged with an initial immersion height and then move upwards from calm water. The pressure distribution along the wetted surface of the body is the focus of this research. The snapshot POD is applied to the database including a group of pressure field snapshots captured at a certain time interval. By

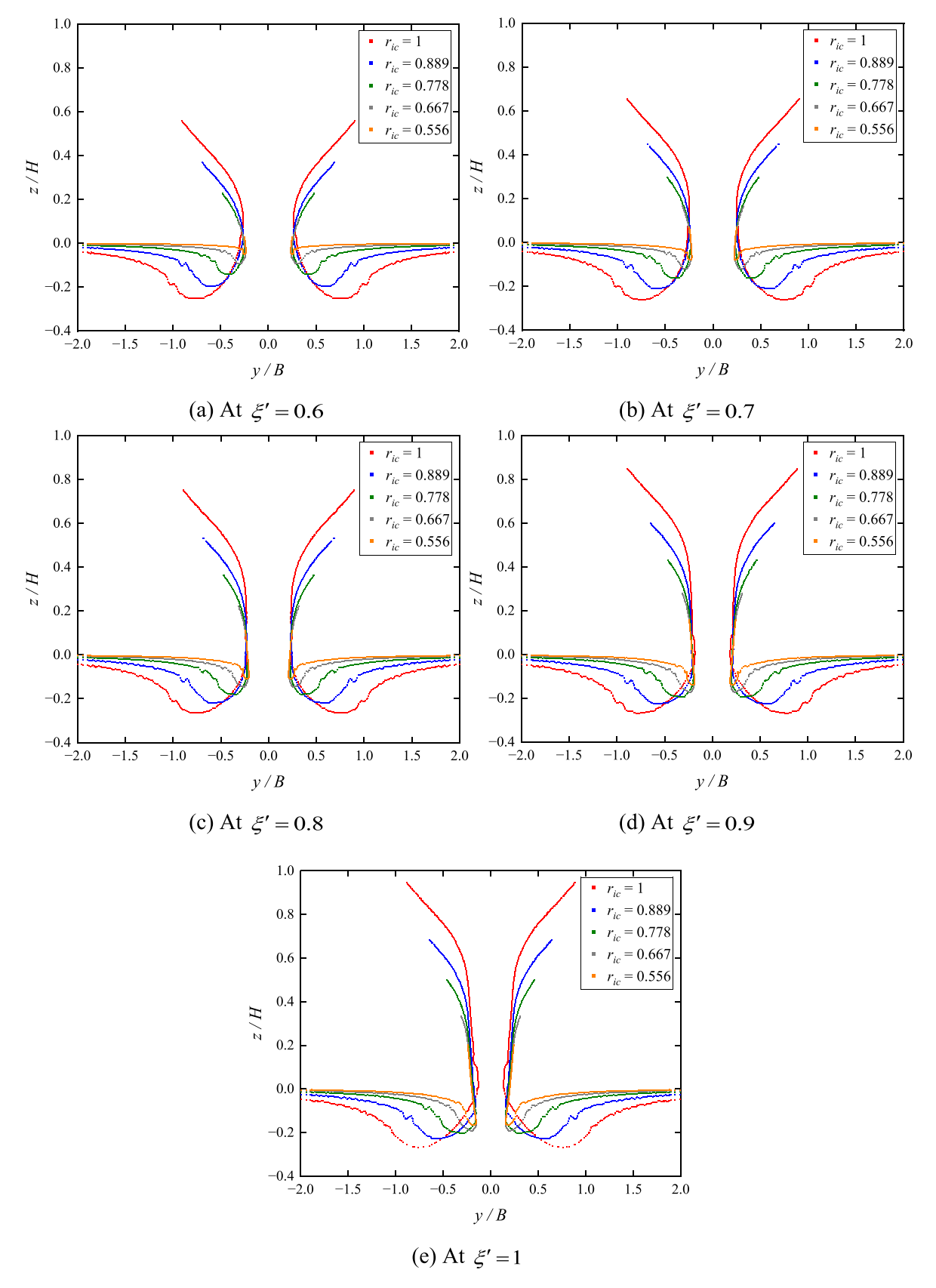


Fig. 19. Free surface profiles around the ship section model under different initial immersion conditions.

Table 9Detailed information on the test water exit case for the assessment of the proposed empirical approach.

Model	Case No.	Immersion condition r_{ic}	Acceleration a
Ship section	27	0.944	98 - 3200/9 × t m/s ²

identifying dominant POD basis modes from the perspective of energy, the full dimensions of a complicated water exit problem can be significantly reduced, resulting in the order reduction. In this context, the pressure distribution along the body wetted surface can be estimated using a group of POD basis modes and their corresponding time coefficients, with preserving essential dynamic features.

Two different body shapes are studied in this paper, namely the typical wedge model and the practical ship section model. Water exit cases featured different initial immersion conditions and constant body accelerations are imposed on both body models. The CFD software STAR-CCM+ is used to collect numerical results of the pressure distribution and then to construct the high-fidelity database. In addition, the

evolution of the wetted half-width of the body is also obtained from numerical simulations. It is found that two POD basis modes are sufficient for the accurate reconstruction of the pressure distribution for the wedge model, while three POD basis modes are sufficient for the ship section model. The 1st basis mode of the wedge model always contains over 99% of the total energy of the system. In comparison, the energy proportion of the 1st basis mode of the ship section model varies with different initial immersion conditions, but this mode still has a considerable contribution to the pressure distribution. By observing the spatial profile of the mean mode, it is revealed that the position experiencing the greatest average pressure is not at the bottom, which indicates the significant nonlinear effects. Furthermore, neither the initial immersion

 Table 10

 RMSE on the examination of the proposed empirical approach.

Displacement ξ	0.2	0.4	0.6	0.8
RMSE	0.1135	0.1790	0.1627	0.1634

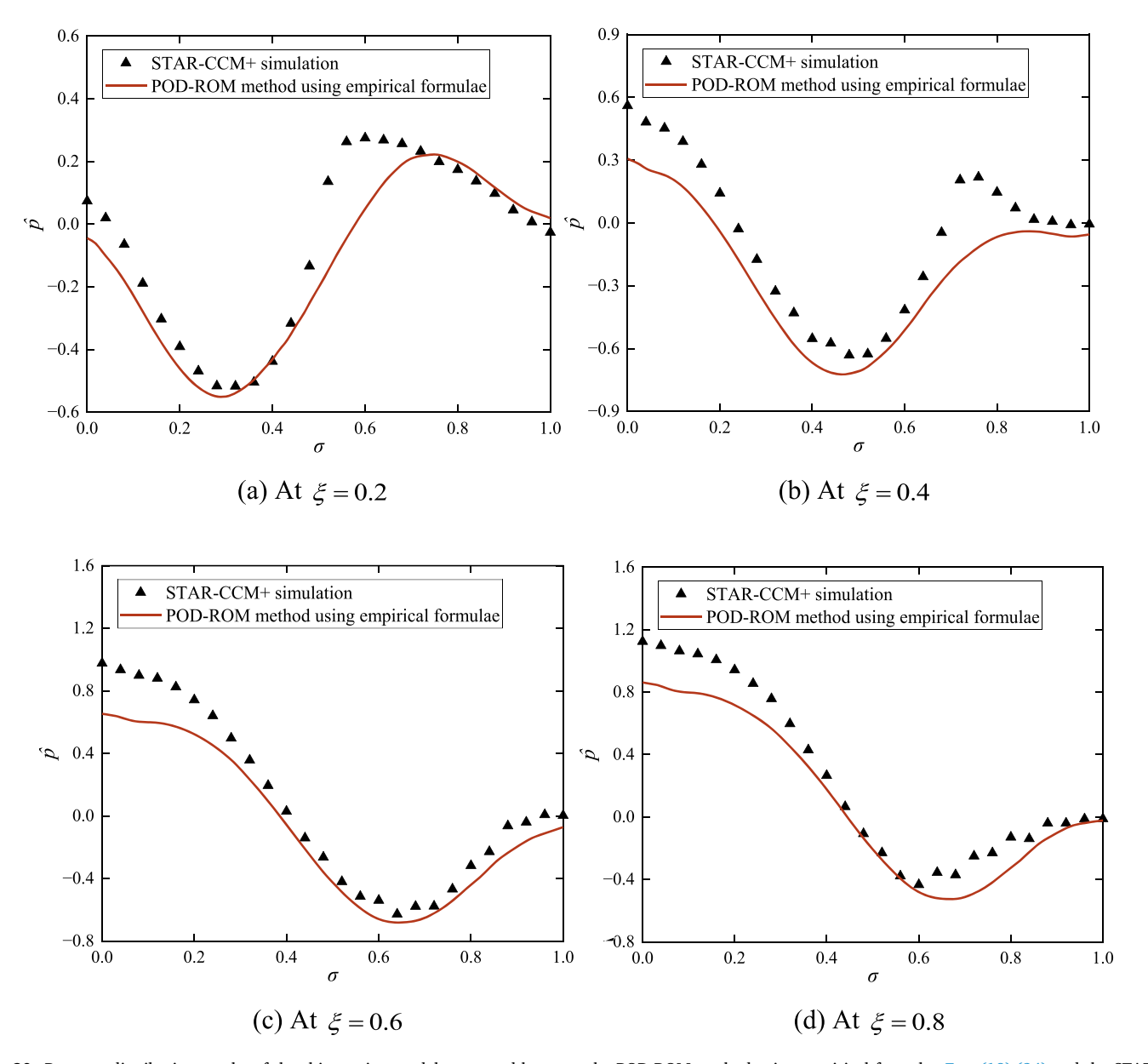


Fig. 20. Pressure distribution results of the ship section model compared between the POD-ROM method using empirical formulae Eqs. (18)-(34) and the STAR-CCM+ simulation.

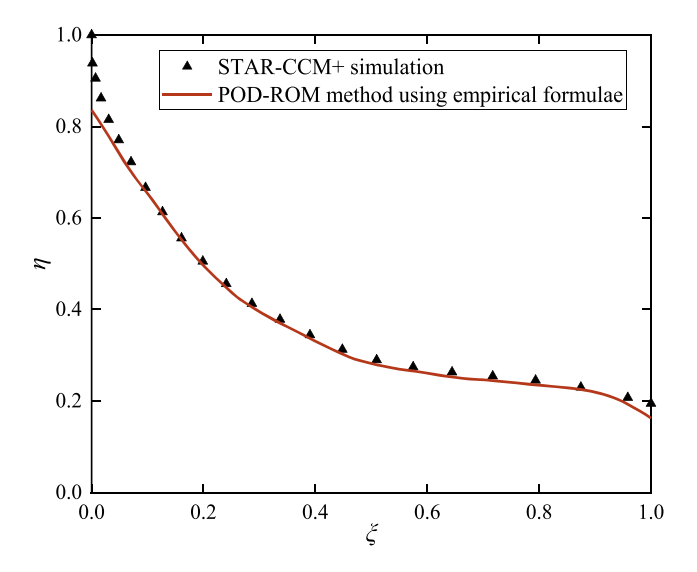


Fig. 21. Evolution results of the wetted half-width of the ship section model compared between the POD-ROM method using empirical formulae Eqs. (18)-(34) and the STAR-CCM+ simulation.

conditions nor the motion state of the body affects the POD functions of the wedge model, while the initial immersion condition has a strong relationship with temporal POD functions of the ship section model.

The application of the POD-ROM method is firstly evaluated by giving each body model an additional test water exit case and examining the pressure distribution provided by this method. Our predictions using a limited number of POD basis modes show a satisfactory agreement with those obtained from CFD simulations. It is also proved that modes accounting for a relatively small proportion of the total energy of the system are indispensable for the accurate results. Furthermore, in order to address the issue that the temporal POD functions of the ship section model vary with different initial immersion conditions, the so-called characteristic evolution patterns are explored and represented by the case with the greatest initial immersion depth. A group of empirical formulae is subsequently proposed to determine the stage and rate of evolution for any unseen water exit case. The validation of the introduced empirical approach is also performed by giving the ship section model an imposed motion with the time-varying body acceleration. The inspiring agreement with numerical results can be found, indicating hydrodynamic loads acting on the body can be rapidly predicted without redundant and time-consuming theoretical calculations or numerical simulations. The applicability of the POD-ROM method in dealing with problems in practical maritime engineering is correspondingly verified.

In the near future, the improvement of empirical formulae for more accurate pressure distribution predictions and the application of the POD-ROM method for 3D water exit problems are expected to be the topics of our following research.

CRediT authorship contribution statement

Xupeng Sui: Writing – original draft, Investigation, Methodology. **Kamal Djidjeli:** Writing – review & editing, Methodology, Validation, Investigation, Supervision, Funding acquisition. **Zhe Sun:** Writing – review & editing, Methodology, Validation, Investigation, Supervision,

Funding acquisition. **Jing Tang Xing:** Supervision, Writing – review & editing.

Declaration of competing interest

The authors declare that they have no known competing financial interests or personal relationships that could have appeared to influence the work reported in this paper.

Acknowledgements

This work is supported by the National Key Research and Development Programme of China (2021YFC2801701 & 2021YFC2801700), National Natural Science Foundation of China (No. 52171295) and National Key Laboratory of Ship Structural Safety of China (Naklas2024KF009-J).

References

Aarsnes, J.V., 1996. Drop test with ship sections – effect of roll angle. Norwegian Marine Technology Research Institute, Trondheim, Norway.

Del Buono, A., Bernardini, G., Tassin, A., Iafrati, A., 2021. Water entry and exit of 2D and axisymmetric bodies. J. Fluids. Struct. 103.

Druault, P., Chaillou, C., 2007. Use of proper orthogonal decomposition for reconstructing the 3D in-cylinder mean-flow field from PIV data. Comptes Rendus Mécanique 335 (1), 42–47.

Fontaine, E., Cointe, R., 1997. A slender body approach to nonlinear bow waves. Philos. Trans. R. Soc. Lond. Series A 355 (1724), 565–574.

Hilberg, D., Lazik, W., Fiedler, H., 1994. The application of classical POD and snapshot POD in a turbulent shear layer with periodic structures. Appl. Scientif. Res. 53 (3), 283–290.

Kaplan, P., 1987. Analysis and prediction of flat bottom slamming impact of advanced marine vehicles in waves. Int. Shipbuild. Progr. 34 (391), 44–53.

Kaplan, P., 1992. Wave impact forces on offshore structures: re-examination and new interpretations. In: Offshore Technology Conference.

Korobkin, A.A., 2013. A linearized model of water exit. J. Fluid. Mech. 737, 368–386.
Korobkin, A.A., Khabakhpasheva, T.I., Maki, K.J., 2017. Hydrodynamic forces in water exit problems. J. Fluids. Struct. 69, 16–33.

Liberge, E., Hamdouni, A., 2010. Reduced order modelling method via proper orthogonal decomposition (POD) for flow around an oscillating cylinder. J. Fluids. Struct. 26 (2), 292–311.

Lumley, J.L., 1967. The structure of inhomogeneous turbulent flows. Atmos. Turbul. Radio Wave Propag. 166–178.

Olbrich, M., Bär, M., Oberleithner, K., Schmelter, S., 2021. Statistical characterization of horizontal slug flow using snapshot proper orthogonal decomposition. Int. J. Multiph. Flow 134, 103453.

Rajavaheinthan, R., Greenhow, M., 2015. Constant acceleration exit of two-dimensional free-surface-piercing bodies. Appl. Ocean Res. 50, 30–46.

Sen, M., Bhaganagar, K., Juttijudata, V., 2007. Application of proper orthogonal decomposition (POD) to investigate a turbulent boundary layer in a channel with rough walls. J. Turbulence (8), N41.

Siegel, S., Cohen, K., Seidel, J., McLaughlin, T., 2006. Proper orthogonal decomposition snapshot selection for state estimation of feedback controlled flows. In: 44th AIAA Aerospace Sciences Meeting and Exhibit, p. 1400.

Sirovich, L., 1987a. Turbulence and the dynamics of coherent structures. I. Coherent structures. Q. Appl. Math. 45 (3), 561–571.

Sirovich, L., 1987b. Turbulence and the dynamics of coherent structures. II. Symmetries and transformations. Q. Appl. Math. 45 (3), 573–582.

Sirovich, L., 1987c. Turbulence and the dynamics of coherent structures. III. Dynamics and scaling. Q. Appl. Math. 45 (3), 583–590.

Sui, X., Djidjeli, K., Sun, Z., Xing, J.T., 2024. Combined force decomposition approach and CFD simulation methods for 2D water entry and exit problem. Ocean Eng. 300, 117421.

Sun, Z., Sui, X.P., Korobkin, A., Zou, L., Zong, Z., 2022. Slamming force decomposition with gravity effect. J. Fluids. Struct. 114.

Tassin, A., Piro, D.J., Korobkin, A.A., Maki, K.J., Cooker, M.J., 2013. Two-dimensional water entry and exit of a body whose shape varies in time. J. Fluids. Struct. 40, 317–336.